

MAGNETIC TUNNEL SPIN INJECTORS FOR SPINTRONICS

A DISSERTATION  
SUBMITTED TO THE DEPARTMENT OF  
ELECTRICAL ENGINEERING  
AND THE COMMITTEE ON GRADUATE STUDIES  
OF STANFORD UNIVERSITY  
IN PARTIAL FULFILLMENT OF THE REQUIREMENTS  
FOR THE DEGREE OF  
DOCTOR OF PHILOSOPHY

Roger Wang  
February 2006

© Copyright by Roger Wang 2006  
All Rights Reserved

# Abstract

Research in electron spin-based electronics, or "spintronics", has a universal goal to develop applications for electron spin in a broad range of electronics and strives to produce low power nanoscale devices. Spin injection into semiconductors is an important initial step in the development of spintronic devices. The primary goal of spin injection is to create a highly spin polarized population of electrons inside a semiconductor at room temperature for study, characterization, and manipulation. This dissertation investigates magnetic tunnel spin injectors that aim to meet the spin injection requirements needed for potential spintronic devices.

Magnetism and spin are inherently related, and chapter 1 provides a detailed introduction of magnetic tunneling and spin polarized electron transport, followed by a summary of the field of spintronics. Chapter 2 then describes the fabrication of the spin injector structures studied in this dissertation, and also illustrates the optical spin detection technique that correlates the measured electroluminescence polarization from quantum wells to the electron spin polarization inside the semiconductor.

Chapter 3 reports the spin injection from the magnetic tunnel transistor (MTT) spin injector, which is capable of producing highly spin polarized tunneling currents through spin selective scattering in its multilayer structure. The MTT achieves a lower bound of  $\sim 10\%$  injected spin polarization at 1.4 K measured from the circularly polarized electroluminescence from InGaAs quantum wells. Chapter 4 reports

spin injection from CoFe-MgO(100) tunnel spin injectors, where spin dependent tunneling through MgO(100) produces highly spin polarized tunneling currents. These structures achieve lower bound injected spin polarizations exceeding 50% at 100 K and 30% at 290 K measured from the circularly polarized electroluminescence from GaAs quantum wells. The CoFe-MgO spin injectors also demonstrate excellent thermal stability, maintaining high injection efficiencies even after exposure to temperatures of up to 400 °C. Bias voltage and temperature dependent studies on these structures indicate a significant dependence of the electroluminescence polarization on the spin and carrier recombination lifetimes inside the semiconductor.

Chapter 5 investigates the spin and carrier lifetime effects on the electroluminescence polarization using time resolved optical techniques. These studies suggest that a peak in the recombination lifetime with temperature is responsible for the nonmonotonic temperature dependence observed in the electroluminescence polarization, and that the initially injected spin polarization from CoFe-MgO spin injectors is a nearly temperature independent  $\sim 70\%$  from 10 K up to room temperature.

# Acknowledgments

First, I would like to thank Stuart Parkin, not only for his knowledge and advice, but for his infinite supply of optimism and energy which is invaluable in the unpredictable world of research often characterized by disappointing (or no) results and broken equipment. I thank James Harris for his guidance and his enthusiasm in recruiting me for research. I am also indebted to Xin Jiang, who was my mentor and taught me almost everything I know in terms of research.

In addition, I thank Dwight Nishimura for his encouragement and kindness during the inevitable struggles and trials of the first year EE student. On a similar note, I am deeply grateful for the tutelage and friendship of Sotirios Limotyrakis, who provided me with several crash courses in a number of areas in electrical engineering, most notably analog circuit design. His time and effort helped me bridge the large gap between my non-EE undergraduate degree and the competitive expectations of the EE graduate program at Stanford.

I acknowledge my colleagues in my dissertation project: Xin Jiang, Bob Shelby for his help with the optical measurements, Roger MacFarlane who also aided in the optical studies, Glenn Solomon for useful discussions and quantum well samples, Seth Bank for growing excellent quantum well samples, Gian Salis for the time-resolved experiment collaboration, and Anthony Ndirango who provided a fundamental understanding to the physics involved in the project.

I acknowledge the other members of the Parkin Group at IBM Almaden, past and

present, who have played a role in my research one way or another: Alex Panchula for his friendly advice and humor, Christian Kaiser for his funny stories and his expertise with the bonding machine, Kevin Roche who simply keeps everything running, Brian Hughes for his humorous opinions on anything from a new tool component to Mel Gibson's Braveheart and for keeping the deposition tools up and running, See-hun Yang for his help with the deposition tools, Mahesh Samant for all his patience and willingness to buy things I break, and Guenole Jan for his immense scientific knowledge and mechanical know-how. I wish Hyunsoo Yang, Rekha Rajaram, Masamitsu Hayashi all the best in completing their PhD projects. I also wish Anjia Gu, Li Gao, and Cheng-han Yang the best of luck as they begin new projects within the group.

I thank Walt Harrison for reading my thesis and proofing the theoretical aspects of my work. I also thank the rest of the Harris Group who sat patiently through many of my group talks and provided feedback. I acknowledge the rest of the Parkin group, who all play a key role in keeping research within the group at a world class level. I thank the Noyce Foundation for their financial support through the Stanford Graduate Fellowship, and the National Science Foundation for their financial aid.

Finally, my PhD journey would not have been enjoyable without the company and endless support of my friends and family. I thank Scott Kulchycki for just about everything, and Alok Aggarwal for helping keep my computer alive. I thank my parents for their patience, understanding, and many needed home cooked meals. Last, and furthest from least, I thank my wife Charlotte for her love, support, and comfort.

# Contents

Abstract	iii
Acknowledgments	v
<b>1 Magnetic Tunneling and Spin Injection</b>	<b>1</b>
1.1 Magnetic Tunneling . . . . .	1
1.1.1 History . . . . .	1
1.1.2 Jullière Model: “Simple” Magnetic Tunneling Theory . . . . .	4
1.1.3 Two Types of Magnetic Tunnel Junctions . . . . .	8
1.1.4 The Magnetic Tunnel Transistor (MTT) . . . . .	11
1.2 Semiconductor Spintronics and Spin Injection . . . . .	14
1.2.1 Spintronics . . . . .	14
1.2.2 Spin Injection . . . . .	16
1.2.3 Spin Relaxation . . . . .	17
1.2.4 Spin Relaxation Mechanisms . . . . .	22
<b>2 Injector Growth and Spin Detection</b>	<b>25</b>
2.1 Spin Injector Fabrication . . . . .	25
2.2 Optical Detection of Spin Polarization . . . . .	28
2.2.1 Optical Selection Rules . . . . .	28

2.2.2	Optical Detection Setup . . . . .	31
<b>3</b>	<b>Magnetic Tunnel Transistor Spin Injector</b>	<b>33</b>
3.1	Introduction . . . . .	33
3.2	MTT-Spin LED Fabrication . . . . .	34
3.3	Electroluminescence Spectra and Polarization . . . . .	37
3.4	Polarization Dependence on Magnetic Field . . . . .	40
3.5	Polarization Dependence on Collector-Base Bias . . . . .	42
3.6	Summary . . . . .	44
<b>4</b>	<b>CoFe-MgO(100) Tunnel Spin Injector</b>	<b>45</b>
4.1	Introduction . . . . .	46
4.2	Injector-Spin LED Fabrication . . . . .	47
4.3	CoFe-MgO on Al <sub>0.08</sub> Ga <sub>0.92</sub> As-GaAs . . . . .	50
4.3.1	Electroluminescence Measurements . . . . .	50
4.3.2	Bias Voltage and Temperature Effects . . . . .	54
4.3.3	Thermal Annealing and Stability . . . . .	60
4.4	CoFe-MgO on Al <sub>0.16</sub> Ga <sub>0.84</sub> As-GaAs . . . . .	63
4.4.1	Electroluminescence Measurements . . . . .	63
4.4.2	Bias Voltage and Temperature Effects . . . . .	65
4.5	Summary . . . . .	68
<b>5</b>	<b>Spin and Recombination Lifetime Effects</b>	<b>71</b>
5.1	Introduction . . . . .	72
5.1.1	Temperature dependence of spin lifetime . . . . .	72
5.1.2	Temperature dependence of recombination lifetime . . . . .	74
5.2	Time Resolved Optical Studies . . . . .	75
5.3	Experimental Setup . . . . .	77

5.4	Experimental Results and Discussion . . . . .	77
5.5	Summary . . . . .	81
<b>6</b>	<b>Conclusion</b>	<b>83</b>
<b>A</b>	<b>D'yakonov-Perel' spin relaxation in GaAs</b>	<b>89</b>
A.1	Derivation of Equation 5.3 . . . . .	89
	<b>Bibliography</b>	<b>95</b>



# List of Figures

1.1	A standard MTJ. . . . .	2
1.2	Two resistance modes for the MTJ. . . . .	5
1.3	Density of states schematic for tunneling electrons in the parallel and antiparallel alignment modes of the MTJ. . . . .	6
1.4	Hysteresis loop sketch of two FM layers with differing coercivities. . .	9
1.5	A schematic description of a pinned MTJ. . . . .	10
1.6	Energy band diagram of a spin-valve transistor. . . . .	11
1.7	Band diagram of a single base MTT. . . . .	12
1.8	Current vs. magnetic field for a single base MTT. . . . .	14
2.1	Photograph of the magnetron sputtering deposition system used to grow MTT and CoFe-MgO tunnel spin injectors. . . . .	26
2.2	Top view drawing of the MTT and CoFe-MgO spin injectors. . . . .	26
2.3	Top view photograph of a MTT. . . . .	27
2.4	E vs. k band diagram for bulk GaAs around the $\Gamma$ point. . . . .	29
2.5	Optical recombination selection rules in the Faraday geometry. . . . .	30
2.6	Experimental setup for optical studies of spin injection. . . . .	31
3.1	Band diagram of an MTT on a GaAs-InGaAs spin detector LED. . .	35
3.2	Electroluminescence spectra for selected magnetic fields at 1.4 K. . .	38

3.3	Schematic energy representation of spin states under positive magnetic field based on the Zeeman equation. . . . .	38
3.4	Electroluminescence polarization as a function of magnetic field at 1.4 K. . . . .	40
3.5	Collector-to-base bias dependence of electroluminescence polarization and intensity at 1.4 K and 2.5 T. . . . .	42
4.1	Band diagram of a CoFe-MgO spin injector grown on an AlGaAs-GaAs spin LED structure. . . . .	48
4.2	XTEM image of a CoFe-MgO spin injector sputter deposited on GaAs. . . . .	48
4.3	Electroluminescence spectra for selected magnetic fields at 100 K. . . . .	51
4.4	Electroluminescence polarization vs. magnetic field at 100 K for a CoFe-MgO   <i>n-i-p</i> spin LED sample. . . . .	52
4.5	$P_C$ vs. bias voltage for both 8% Al <i>n-i-p</i> and <i>p-i-p</i> samples over a 1.4-100 K temperature range. . . . .	55
4.6	Current-voltage characteristics for an 8% Al <i>n-i-p</i> sample. . . . .	56
4.7	$P_C$ vs. temperature for both <i>n-i-p</i> and <i>p-i-p</i> samples with 8% Al doped barriers at a given bias voltage. . . . .	57
4.8	Electroluminescence polarization vs. temperature at $V_T = 1.8$ V for an 8% Al <i>n-i-p</i> sample. . . . .	59
4.9	Improvement in electroluminescence polarization with thermal annealing for an 8% Al <i>n-i-p</i> sample. . . . .	61
4.10	$P_C$ vs. temperature for an 8% Al <i>n-i-p</i> sample after annealing at various temperatures. . . . .	61
4.11	Electroluminescence spectra at 5, 0, and -5 T for a 16% Al <i>p-i-p</i> sample at 290 K and $V_T = 2.0$ V. . . . .	63
4.12	Electroluminescence polarization vs. magnetic field at 290 K with $V_T = 2.0$ V for a 16% Al <i>p-i-p</i> sample. . . . .	64

4.13	$P_C$ vs. bias voltage at selected temperatures for a 16% Al $p-i-p$ sample.	65
4.14	Electroluminescence polarization vs. temperature at $V_T = 2.0$ V for a 16% Al $p-i-p$ sample. . . . .	66
4.15	Background polarization signal vs. temperature for a 16% Al $p-i-p$ sample with $V_T = 2.0$ V. . . . .	67
4.16	Current vs. temperature in a 16% Al $p-i-p$ sample with $V_T = 2.0$ V. . . . .	67
5.1	Integrated electroluminescence intensity vs. temperature for an 8% Al $p-i-p$ sample. . . . .	75
5.2	Illustration of the time resolved Kerr rotation measurement. . . . .	76
5.3	Time resolved Kerr rotation and differential reflectivity for a 16% Al $p-i-p$ sample. . . . .	78
5.4	Measured spin and carrier lifetimes, and expected polarization for a 16% Al $p-i-p$ sample. . . . .	79
5.5	Measured spin and carrier lifetimes, and expected polarization for a 8% Al $p-i-p$ sample. . . . .	80
6.1	Achieved spin injection from various spin injector sources. . . . .	86



# Chapter 1

## Magnetic Tunneling and Spin Injection

The magnetic tunnel spin injectors described in this dissertation follow an extensive history of research in magnetic tunneling and spin polarized current, and a brief summary of the field is included in the first part of this introductory chapter. The second part of the chapter reviews spin injection, which combines aspects of magnetism, optics, and spin physics altogether in a semiconductor setting.

### 1.1 Magnetic Tunneling

#### 1.1.1 History

In the early 1970's, P. M. Tedrow and R. Meservey measured the spin polarization of electrons tunneling from ferromagnetic metals (Fe, Co, Ni, and Gd) through aluminum oxide ( $\text{Al}_2\text{O}_3$ ) into superconducting aluminum metal under an external magnetic field [1]. The spin polarization of the tunneling electrons was found to be dependent on the magnetic orientation of the ferromagnetic materials, which could be

manipulated by an applied magnetic field. In addition, from studies on Al | Al<sub>2</sub>O<sub>3</sub> | Al junctions under high external magnetic fields, the tunneling process was found to be spin conserving [2].

These experiments suggested that by manipulating the magnetization of the ferromagnetic layers, one could control the tunneling current in a ferromagnetic metal-insulator-ferromagnetic metal junction (FM|I|FM). This effect was first measured by Jullière in 1975, who found a change in tunneling current of 14 % at 4.2 K in a Co | amorphous-Ge | Fe junction [3]. Jullière proposed a simple model for the measured effect:

$$\frac{\Delta G}{G_p} = \frac{G_p - G_{ap}}{G_p} = \frac{2P_1P_2}{1 + P_1P_2} \quad (1.1)$$

where  $G$  is the junction conductance ( $p$ -parallel,  $ap$ -antiparallel alignment of the FM layers), and  $P_1$  and  $P_2$  represents the spin polarization of the two FM layers. The polarization within a FM layer is given by:

$$P_{layer} = \frac{N_{\uparrow} - N_{\downarrow}}{N_{\uparrow} + N_{\downarrow}} \quad (1.2)$$

where  $N_{\uparrow(\downarrow)}$  are the Fermi level density of states of majority (minority) spin electrons in the layer [3]. Later experiments with amorphous Ge as a tunneling barrier failed to produce spin polarized transport [4], and researchers were unable to reproduce Jullière's results.



Figure 1.1: A standard MTJ.

Nevertheless, the Jullière model remains useful for characterizing spin dependent current effects in FM|I|FM junctions. The change in junction resistance deriving from the relative alignment of the FM layer magnetizations in a FM|I|FM junction is termed magnetoresistance (MR), and generally expressed in one of two forms:

$$\textit{Tunnel Magnetoresistance (TMR)} = \frac{\Delta R}{R_p} = \frac{R_{ap} - R_p}{R_p} = \frac{2P_1P_2}{1 - P_1P_2} \quad (1.3)$$

$$\textit{Junction Magnetoresistance (JMR)} = \frac{\Delta R}{R_{ap}} = \frac{R_{ap} - R_p}{R_{ap}} = \frac{2P_1P_2}{1 + P_1P_2} \quad (1.4)$$

where  $R$  is the resistance across the FM|I|FM structure. Both TMR and JMR are valid descriptions of the magnetoresistive effect and choice of either representation is based on preference. The FM|I|FM junction, shown in fig. 1.1, is called the magnetic tunnel junction (MTJ). The electrical current in the MTJ travels perpendicular to the film plane (CPP) of the FM layers, where the FM layers act as electrodes.

Although MTJs remained an interesting and intense research topic since their discovery in the early 1970's, not until 1995 were significant MR values reported at room temperature. Miyazaki and Tezuka reported JMR values of 30% at 4.2 K and 18% at 300 K [5], although these results were later disputed when considering geometrical nonlinear current flow effects [6]. Moodera et al. observed JMR values of 24%, 20%, and 11.8% at 4.2, 77, and 295 K, respectively, using CoFe|Al<sub>2</sub>O<sub>3</sub>|Co and CoFe|Al<sub>2</sub>O<sub>3</sub>|NiFe junctions [7]. The primary reasons for the improvement in MR value and stability were the advances made in deposition and fabrication of the junction devices. The ability to grow thin, smooth FM films and insulating layers largely determines the operating capabilities of the final device. With modern day deposition techniques, room temperature commercial devices based on the MTJ have become a realistic possibility.

Several applications for MTJ devices have drawn significant interest. The MTJ

has a possible application as a hard drive read sensor [8], where the goal is to exploit the compactness and higher signal from a CPP MTJ as an improvement over existing current-in-plane Giant Magnetoresistance (GMR) [9] devices. Another potential application is the implementation of the MTJ in magnetic random access memory (MRAM). MRAM is a proposed memory technology offering nonvolatility (retaining information even when the power is removed), high speed (projected to be faster than both nonvolatile Flash RAM, and popular Dynamic RAM which requires a refresh after each read), and high densities matching DRAM densities. Techniques for building MRAM cells have been of interest for decades [10, 11], and the use of both anisotropic MR [12] and GMR [13] have been proposed. However, today the MTJ remains both theoretically and practically the most promising structure for use in MRAM technologies [14, 15].

### 1.1.2 Jullière Model: “Simple” Magnetic Tunneling Theory

The backbone of MTJ functionality is magnetoresistance—the change of resistance (or current) across the junction when the magnetizations of the two FM layers are parallel relative to antiparallel aligned. Typically, when the two magnetizations have parallel alignment, the MTJ is in a low resistance ( $R_p$ ) or high current mode, and under antiparallel alignment, the MTJ is in a high resistance ( $R_{ap}$ ) or low current mode (see fig. 1.2). An easy approach to understanding the function of the two magnetic layers is to describe the bottom FM layer in fig. 1.2 as a spin filter, creating a current of electrons with primarily one spin orientation. The top FM layer in fig. 1.2 acts as a spin detector, favoring one spin orientation (conventionally defined as the majority spin) of electrons to tunnel and continue as current. In addition, conductance through the FM materials can be viewed as a summation of two independent and unequal components based on spin, or in other words, the sum of two spin polarized currents [16–19].

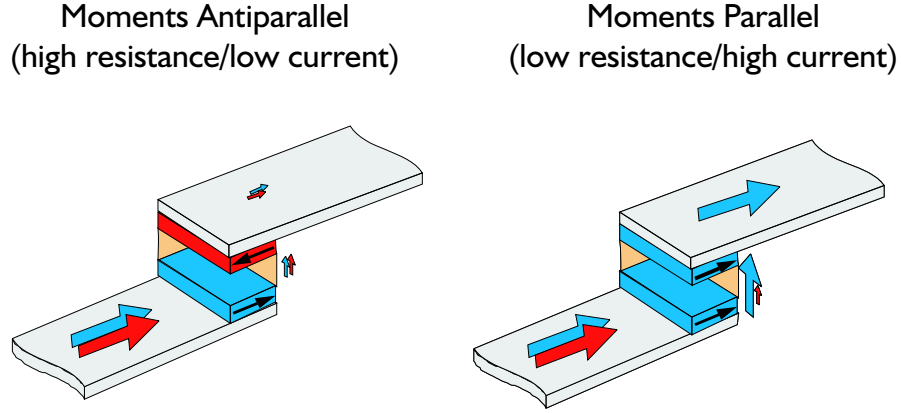


Figure 1.2: Typical MTJ operation where the bottom FM layer acts as a spin filter, and the top FM layer acts as a spin detector. When the magnetizations of the two FM layers are antiparallel, the MTJ is in a low current, high resistance mode. When the magnetizations are parallel, the MTJ is in a high current, low resistance mode.

Jullière's model [3] describes the zero bias voltage magnetoresistive effect using the Fermi level density of states of the spin orientations in each FM layer. Since tunneling in the MTJ is spin conserving [2], an electron of one spin state in the first FM layer can only tunnel to an available identical spin state in the second FM layer. Figure 1.3 illustrates this process when there is a larger majority spin density of states at the Fermi level than minority spin density of states. When the two FM layers are aligned, the large number of majority spin electrons in the first FM layer can tunnel freely to the large density of states available for the same spin in the second FM layer (both layers have the same majority spin orientation). In the parallel, low resistance (high current) state, the current,  $I_p$ , is proportional to:

$$I_p \approx N_{\uparrow}^1 N_{\uparrow}^2 + N_{\downarrow}^1 N_{\downarrow}^2 \quad (1.5)$$

where  $N_{\uparrow(\downarrow)}^1$  refers to the Fermi level density of states of the majority (minority) spin orientation in the first FM layer and  $N_{\uparrow(\downarrow)}^2$  refers to the Fermi level density of states

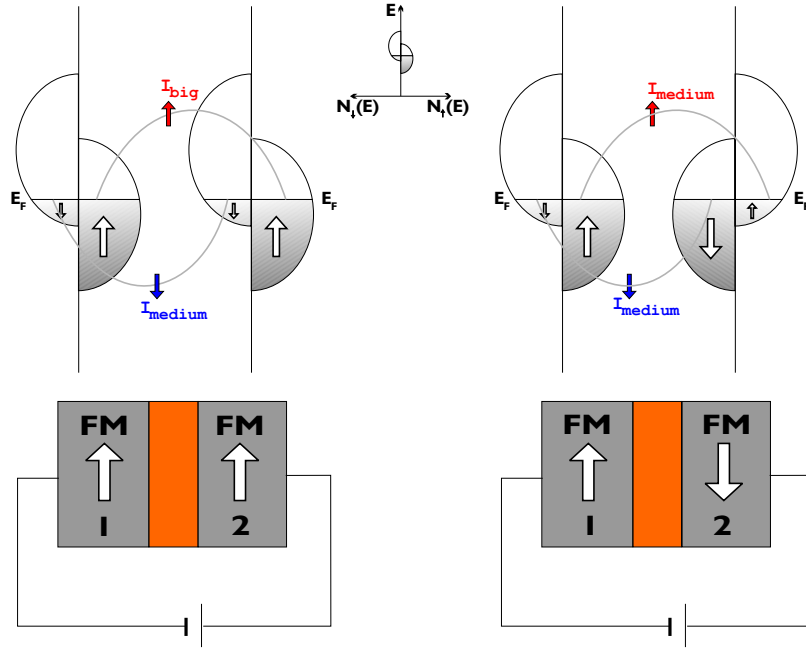


Figure 1.3: Density of states schematic for tunneling electrons in the parallel (left) and antiparallel (right) alignment modes of the MTJ.

in the second FM layer (numerical referencing of the FM layers as defined in fig. 1.3). Under parallel alignment of the FM layers, the tunneling current is spin polarized with a polarization given by:

$$P = \frac{n_{\uparrow} - n_{\downarrow}}{n_{\uparrow} + n_{\downarrow}} \quad (1.6)$$

where  $n_{\uparrow(\downarrow)}$  refers to the number of majority (minority) spin electrons. For this dissertation, the term “spin polarization” of an electron population refers to eqn. 1.6.

For antiparallel alignment, the majority spin electrons in the first FM layer are minority spin electrons in the second FM layer. Thus, the small minority spin states of the second FM layer limit the tunneling of the large number of majority spin electrons in the first FM layer. Only the smaller number of minority spin electrons from the first FM layer can tunnel freely to the majority spin states in the second FM

layer. Under antiparallel alignment, the tunneling current,  $I_{ap}$ , is proportional as:

$$I_{ap} \approx N_{\uparrow}^1 N_{\downarrow}^2 + N_{\downarrow}^1 N_{\uparrow}^2 \quad (1.7)$$

In the antiparallel case, the tunneling current is not spin polarized.

Note that in fig. 1.3, the density of states for each spin orientation in a FM layer are drawn shifted relative to each other due to the exchange interaction (also called exchange splitting). This effect arises when the Fermi level lies in an energetically narrow electron band that has a high density of states at the Fermi level (e.g. the 3d band of a transition metal like nickel). In this case, it is energetically favorable for the electrons to have the same spin, thereby minimizing their Coulomb energy, and resulting in a lower energy for the electrons of one spin orientation. Opposing this effect is the band energy needed to place two electrons in different states but with the same spin instead of two electrons in one state with opposite spins. This band energy is greater than the Coulomb energy if the Fermi level lies in an energetically broad electron band with a low density of states at the Fermi level (e.g. the 4s band in copper).

For academic interest, the Jullière model, though often used in analyzing MTJs, is not rigorous. It assumes single domain magnetization and does not include several factors such as the effects of bias voltage, temperature, disorder, and tunneling matrix elements. Theoretical characterization and modeling of magnetic tunneling continues to be an active field of research. For example, Zhang et al. have modeled the bias voltage dependence of MR in MTJs, attributing the sharp decrease in MR at very low biases to magnon scattering, and deriving expressions for the parallel and antiparallel conductance [20]. MacDonald et al. have modeled the temperature dependence of MR, predicting a  $T^{3/2}$  behavior where the spin polarization is proportional to the magnetization of the FM layer. Complimentary to the Jullière model, Slonczewski

has modeled a FM|I|FM structure in a quantum mechanical system using a free electron approach [21] and has also studied the effect of disorder [22] in MTJs on the tunneling conductance. Theoretical predictions of exceedingly high MR in MTJs with MgO(100) tunnel barriers have been reported by both Mathon and Umerski [23] and Butler et al. [24,25].

Another topic of continuing interest is the positive polarization (majority spin dominant transport) measured in the superconducting tunneling microscopy experiments of Tedrow and Meservey [1,26], which does not match theoretical calculations for Co and Ni that show a higher density of states for the minority  $d$ -orbital electrons at the Fermi level [27]. Extensive reviews of research in MTJs are available in Refs. [6,28].

### 1.1.3 Two Types of Magnetic Tunnel Junctions

The need to control either parallel or antiparallel alignment of the two FM layers with an external magnetic field in useful devices yields two main types of MTJ structures. The first type of MTJ consists of two FM layers having different coercivities, where the coercivity of a FM layer is defined as the magnetic field where the layer switches its magnetization direction. The second type of MTJ contains a “pinned” FM layer (its magnetization is pinned in a specific direction) and a “free” layer (its magnetization can change with an external magnetic field). Note, the magnetization of a FM layer will saturate when all magnetic moments within the layer become aligned in a single direction, either by pinning or by an external magnetic field bias. Materials with magnetic anisotropy favoring a particular magnetization axis, or easy axis, will display hysteresis in their magnetization under an external magnetic field sweep. A detailed background in magnetic principles and materials is available in Ref. [29].

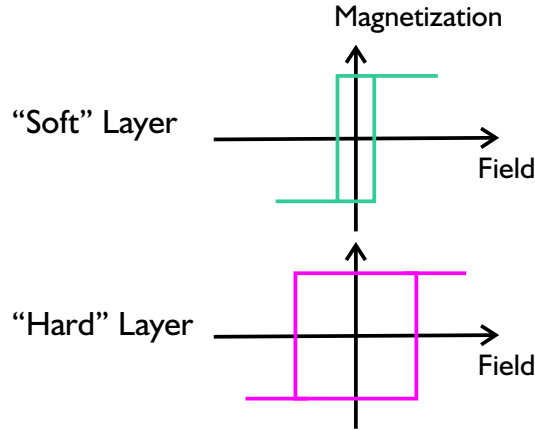


Figure 1.4: Hysteresis loop sketch of two FM layers with differing coercivities assuming the applied magnetic field along the easy axis of the FM layers.

The following sections describe two types of MTJs assuming positive TMR functionality, where the junction is in its low (high) resistance mode when the magnetizations of the FM layers are parallel (antiparallel). Negative TMR exists when the junction resistance is high (low) when the magnetizations of the FM layers are parallel (antiparallel). Examples of negative TMR include structures with  $\text{Al}_2\text{O}_3\text{-Ta}_2\text{O}_5$  barriers [30] and  $\text{Co}|\text{SrTiO}_3|\text{La}_{0.7}\text{Sr}_{0.3}\text{MnO}_3$  junctions [31].

### MTJ Type 1: FM layers with separate coercivities

One type of MTJ, with magnetization curves of its two FM layers shown in fig. 1.4, uses FM layers of differing coercivities and changes resistance when an external magnetic field is swept between the two coercivity values. Starting at a sufficiently high magnetic field, both FM layers are aligned with the field and the MTJ is in its low resistance mode. Decreasing the applied field to zero and then increasing it in the opposite direction first switches the magnetization of the FM layer with the lower coercivity, denoted the soft layer. After switching the soft layer, the FM layers are antiparallel and the MTJ switches to its high resistance mode. Continuing to increase

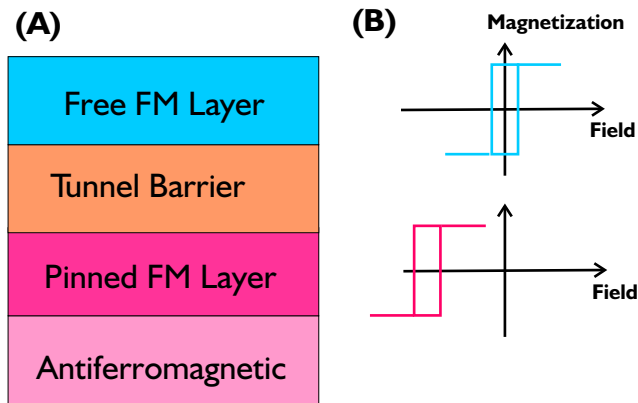


Figure 1.5: A) Schematic of a pinned MTJ with an antiferromagnetic pinning layer. B) Hysteresis loop diagrams, with the applied magnetic field along the easy axis of the layers, of the free and pinned FM layers with each sketch drawn next to their corresponding layers in (A).

the magnetic field eventually switches the magnetization of the other FM layer, denoted the hard layer, and the MTJ switches back to its low resistance state. As a result, the MTJ has a high resistance value when the external magnetic field falls between the coercivities of the two FM layers and a low resistance value otherwise.

### MTJ Type 2: A magnetically pinned FM layer and a free FM layer

Today, the MTJ shown in fig. 1.5 is generally regarded as the frontrunner for MRAM device applications. This type of MTJ uses an antiferromagnetic layer to pin the magnetization of one of the FM layers [29, 32]. The exchange interaction between the antiferromagnetic layer and a FM layer of the MTJ magnetically hardens the FM layer, adding a large offset to its coercivity. The other "free" layer remains unaffected by the antiferromagnetic layer. The magnetization of the pinned layer remains fixed over the range of the applied magnetic field and can only be switched under a field much higher than that used during device operation. Thus, the MTJ can switch from a low resistance mode to a high resistance mode in small magnetic fields through

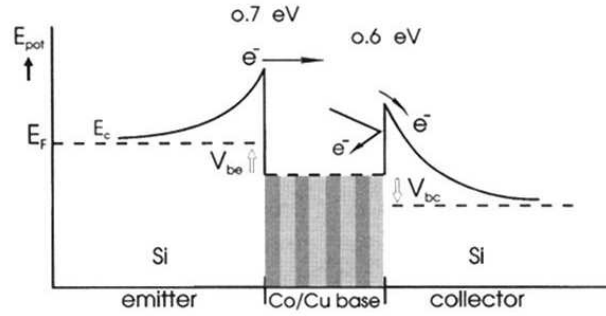


Figure 1.6: Energy band schematic of a spin-valve transistor [45].

switching of the magnetization of the free layer, which has a low coercivity. This type of MTJ shows promise for applications in future MTJ based device technologies such as magnetic disk drive recording read heads and MRAM.

#### 1.1.4 The Magnetic Tunnel Transistor (MTT)

In the quest for fully integrated device technologies utilizing spin information, spin dependent hot electron transport has become an interesting topic in the study of magnetoelectronic devices [33–46]. These devices have high and low resistance modes determined by the alignment of electron spin states. One such hot electron spin device is the spin-valve transistor (SVT) [45, 46]. A SVT, shown in fig. 1.6, consists of a spin-valve base multilayer sandwiched between two semiconductors, which form emitter and collector Schottky barriers with the base layer metals. The base layer generally consists of two FM layers separated by a spacer metal layer such as Cu or Au. Fabrication of the multilayer spin-valve base is essential to the operation of the SVT device as the collector current ( $I_C$ ) that flows across the emitter-base-collector SVT structure depends on the magnetization alignment of the FM base layers. The change in collector current, called magnetocurrent (MC), deriving from the relative alignment of the base layer FM moments has been reported as high as 300% at room

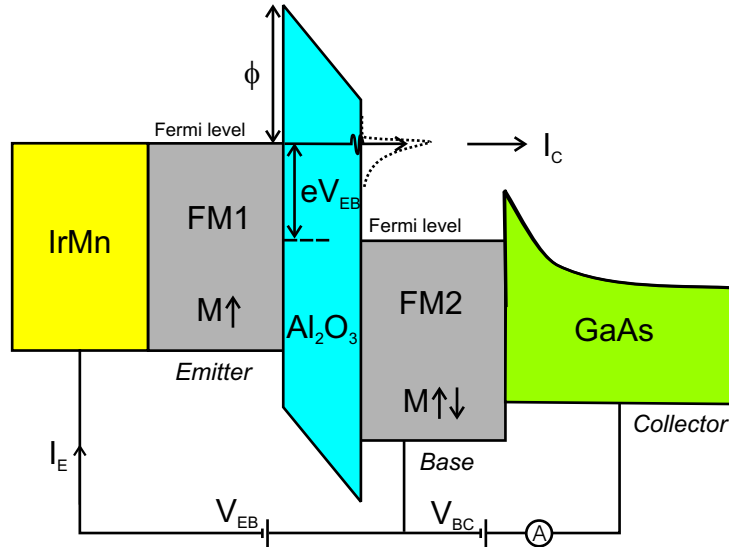


Figure 1.7: Band diagram of a single base MTT. Here, IrMn is the antiferromagnetic material that pins the emitter magnetization.

temperature [47]. While the SVT is an interesting spin-based structure, the device has only limited control over the energy of the hot electron current since the emitter-base Schottky barrier sets the electron energy.

In response to the SVT electron energy limitation, an adapted design having a metal-oxide emitter in place of the original semiconductor emitter offers direct control over the hot electron energy via tunneling from the emitter to the base layer [48, 49]. This device has become known as the magnetic tunnel transistor (MTT), and is essentially a MTJ grown on a semiconductor collector. A band diagram of the MTT is shown in figure 1.7. The MTT is a three terminal device, having electrode contacts at the emitter, base, and collector. The base layer is grown directly on the collector. Then a tunnel oxide is deposited on the base layer, and an emitter FM layer completes the MTJ structure on the semiconductor. In fig. 1.7, the additional layer on top of the emitter layer is an IrMn antiferromagnetic layer, which pins the magnetization of the emitter.

The basic functioning of the MTT device is determined by two bias voltages, the emitter-to-base bias ( $V_{EB}$ ), which controls the current tunneling from the emitter to the base layer, and the collector-to-base bias ( $V_{CB}$ ), which controls the band bending of the Schottky barrier between the base and collector. The pinned emitter injects spin polarized electrons into the base, where the electrons then experience highly spin dependent scattering determined by the magnetization of the base layer [33–41, 45, 46, 50–52]. Generally, electrons with spin parallel to the majority spin of the base layer are scattered to a lesser degree than those with an antiparallel spin. An external magnetic field controls the magnetization of the base layer, and thus determines the electron spin transport across the base. Only electrons that retain sufficient energy to overcome the Schottky barrier at the base-collector interface are collected as current. As a result, the MTT has a magnetocurrent effect similar to the MR effect in the standard MTJ:

$$\text{Magnetocurrent} = \frac{I_{C,P} - I_{C,AP}}{I_{C,AP}} \quad (1.8)$$

where  $I_{C,P}$  and  $I_{C,AP}$  represent the collector current for parallel and antiparallel alignment of the FM layers, respectively. The MTT collector current has a low value when the emitter and base have antiparallel magnetizations, and a high value when the two magnetizations are parallel. Figure 1.8, taken from Dijken et al. [53], shows the collector current behavior with magnetic field in a MTT with CoFe as the FM electrodes.

Extensive studies have measured large magnetocurrent values exceeding 3400% at 77 K for an MTT with a spin-valve base layer [54] and an interesting nonmonotonic emitter-to-base bias voltage dependence of the magnetocurrent for MTTs with GaAs collectors [55, 56]. Hot electron transport in both NiFe and CoFe have been modeled [57] and the effect of nonmagnetic spacer layers in a spin valve base layer has been documented [58]. Finally, functioning MTTs with Si collectors have also been

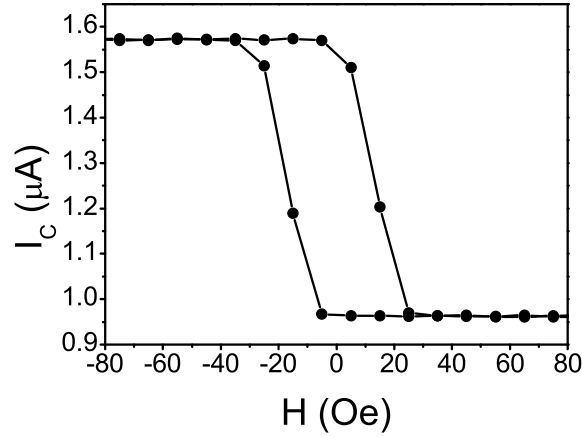


Figure 1.8: Current vs. magnetic field for a single base MTT with CoFe emitter and base layers. The MTT magnetocurrent is 64%, measured at room temperature with an emitter-base bias of 1.4 V and a collector-base bias of 0 V [53].

reported, where various nonmagnetic seed layers were studied as a solution to adverse silicide formation [59].

Overall, the MTT demonstrates significant current modulation based on spin, however a major drawback is the inefficient current transport that results from its multilayer structure. In general, the ratio of the collector current to the emitter to base current in an MTT is  $\sim 10^{-4}$  in the operating range that produces maximum magnetocurrent values [53–58].

## 1.2 Semiconductor Spintronics and Spin Injection

### 1.2.1 Spintronics

Although extensive research on electron spin based phenomena in semiconductors began in the 1960's [60] and a spin-based device had been proposed by Datta and Das in 1990 [61], research in spin-based devices did not draw significant attention until the late 1990's when continued scaling of silicon integrated circuit technology became

increasingly difficult with each subsequent generation. Simultaneously, experimental studies in GaAs demonstrated long spin lifetimes and coherent transport of spin polarized electrons over distances larger than conventional channel lengths [28, 62–64]. These results generated excitement over a possible spin-based device technology, popularly called “spintronics”, where electron spin, rather than electron charge, would be utilized for information processing.

New concepts for spin-based devices have since been proposed [65–67], and one particular area of interest within spintronics has been the spin Hall effect [68–71], where it has been predicted that a dissipationless spin current could exist in the absence of a net charge current [69]. Comprehensive reviews of past, current, and future research, both theoretical and experimental, on spin-based phenomena are summarized in Refs. [28, 72].

One of the major motivations for developing spin-based devices is greater functionality with lower power dissipation, where a spintronic device would aim to transfer and process information utilizing the electron spin, without moving the electron charge. This proposal has drawn significant interest due to the current power consumption issues of conventional electronic technology. The traditional method of improving charge-based computer chips, both clock speed and performance, by shrinking transistor sizes following Moore’s Law (the number of transistors on a chip doubles every 18 to 24 months) has become limited by transistor leakage and power density issues. In short, shrinking transistors increases static power dissipation (while transistors are “off”) as the smaller devices have relatively higher leakage currents. Shrinking transistors to improve computer chips increases both the number of transistors per area and the power dissipation, and thus rapidly increases the overall power density consumption of a chip. This result leads to higher temperatures, which, in turn, leads to even higher transistor leakage and power consumption. The power density problem has led the major computer chip makers including IBM, Sun Microsystems, AMD,

and Intel to shift computer processor design toward multicore processors. A pure spin-based device might resolve the power density issue as the electron spin would be utilized for information processing and require a very low, or even zero, charge flow.

Another motivation for research in spin-based devices derives from the fact that spin is an inherent property of the electron, and nanoscale devices approaching quantum regimes of operation may be able to utilize the spin property of the electron as well as its charge. Also, utilizing spins in a semiconductor environment is advantageous because of the lack of a background population of unpolarized electrons.

### 1.2.2 Spin Injection

In the pursuit for an integrated spin-based semiconductor device technology, the first task is to create a population of spin polarized electrons inside a semiconductor for manipulation, generally referred to as spin injection. An ideal spin injector would demonstrate high injected spin polarization, operate at room temperature, and be both robust and easily fabricated for potential high throughput needs. Such structures would be valuable tools for studying spin transport and dynamics within semiconductors, and could potentially be used as actual components for an eventual spin-based device.

Initial experimental work with dilute magnetic semiconductors has successfully injected spin polarized current into semiconductor collectors [73–77]. However, the magnetic ordering temperatures of these materials are far below room temperature, limiting their potential for applications in realistic spin-based technology. Similarly, ferromagnetic semiconductor spin injectors [78] are currently limited to low temperatures by their low Curie temperatures. For these reasons, FM metals, with Curie temperatures well above room temperature, have drawn significant attention as potential spin injectors. Despite their potential, diffusive injection into semiconductors from FM metals is limited to  $\sim 0.1\%$  by the large conductivity mismatch between

metals and semiconductors [79]. In the diffusive regime, the nonmagnetic semiconductor, which has minimal conductance asymmetry related to spin, will dominate electrical transport due to its high impedance relative to the FM metal. This limitation prevents utilization of ohmic contacts between FM metals and semiconductors as spin injectors. Indeed, efforts using FM diffusive contacts have shown only marginal success [80–82].

In contrast, experimental studies using tunneling contacts such as Schottky tunnel and metal-insulator injectors have reported injected polarizations much higher than the diffusive limit of 0.1% [83–89]. For example, Hanbicki et al. [88] have reported an optically measured 32% spin polarization of injected electrons at 4 K from an Fe-Schottky contact into GaAs, while fully analyzing the tunneling transport across the Schottky barrier. Adelman et al. [89], also using Schottky contacts, have measured up to 6% injected polarization at room temperature. Note that tunneling contacts do not suffer from the conductivity mismatch as the tunneling resistance (recall that tunneling is largely spin conserving [2]) dominates the transport characteristics [90].

### 1.2.3 Spin Relaxation

#### General

Knowledge of spin relaxation, especially in semiconductors, is essential to understanding spin-related effects measured in a semiconductor environment. The origin of spin relaxation can be modeled as a magnetic field contribution to the Bloch Hamiltonian of an electron. For an applied magnetic field, one adds the following expression to the Hamiltonian:

$$\hat{H}_{mag} = \frac{gq\hbar}{2m^*} \boldsymbol{\sigma} \cdot \mathbf{B} \quad (1.9)$$

where  $q$  is the electron charge,  $m^*$  is electron effective mass,  $g$  is the Landé  $g$ -factor, and  $\boldsymbol{\sigma} = (\sigma_x, \sigma_y, \sigma_z)$  are the Pauli matrices. The Bloch Hamiltonian then becomes:

$$\hat{H} = \hat{H}_o + \hat{H}_{mag} \quad (1.10)$$

where  $\hat{H}_o = \frac{\hbar^2 k^2}{2m^*} + V(r)$  and  $\hbar\mathbf{k}$  is the electron momentum. Viewing equations 1.9 and 1.10, one can see that in the absence of a magnetic field, the Pauli matrices do not appear and thus the spin of an electron does not play a role in the Hamiltonian. With this scenario, a population of spin polarized electrons should retain its polarization indefinitely. The empirical knowledge of spin relaxation reveals the presence of a spin dependent term in the Hamiltonian. The question is then: What is the origin of this spin dependent term in the absence of an applied magnetic field?

An illustrative example looks no further than the relativistic (or Lorentz) transformation of the electric and magnetic field on a moving particle [91]:

$$\begin{pmatrix} E'_x \\ E'_y \\ E'_z \end{pmatrix} = \begin{pmatrix} E_x \\ \gamma(E_y - vB_z) \\ \gamma(E_z + vB_y) \end{pmatrix} \quad (1.11)$$

$$\begin{pmatrix} B'_x \\ B'_y \\ B'_z \end{pmatrix} = \begin{pmatrix} B_x \\ \gamma(B_y + \frac{v}{c^2}E_z) \\ \gamma(B_z - \frac{v}{c^2}E_y) \end{pmatrix} \quad (1.12)$$

where the primed coordinate system is the rest frame of the particle, which moves with velocity  $v$  along the  $x$ -axis ( $\mathbf{v} = v\hat{x}$ ) relative to the unprimed lab frame, and

$$\gamma = \frac{1}{\sqrt{1 - v^2/c^2}}$$

with  $c$  being the speed of light. Now, if  $\mathbf{B} = 0$  in the lab frame, from equations 1.11 and 1.12,

$$\mathbf{B}' = -\frac{1}{c^2}(\mathbf{v} \times \mathbf{E}') \quad (1.13)$$

In other words, if the magnetic field equals zero in one frame, an object in any other frame moving at a velocity relative to the first frame will experience a magnetic field described by eqn. 1.13. For completeness, if  $\mathbf{E} = 0$  in the lab frame, equations 1.11 and 1.12 give

$$\mathbf{E}' = (\mathbf{v} \times \mathbf{B}') \quad (1.14)$$

which is the effective electric field providing the well known Lorentz force  $[\mathbf{F} = q(\mathbf{v} \times \mathbf{B})]$  on a charged particle moving in a magnetic field.

Eqn. 1.13 contributes to the Bloch Hamiltonian as the *spin-orbit* term:

$$\hat{H} = \hat{H}_o + \hat{H}_{mag} + \hat{H}_{so}, \quad \hat{H}_{so} = \frac{gq\hbar}{2m^*} \boldsymbol{\sigma} \cdot \left( \frac{\mathbf{v}}{c^2} \times \mathbf{E} \right) \quad (1.15)$$

In the end, the Hamiltonian does not distinguish between a real, applied magnetic field, or something that “looks” like a magnetic field. Any phenomena or effect that appears in the Hamiltonian in the same manner as a magnetic field will act as an effective magnetic field in the system. Here, eqn. 1.15 shows that the spin-orbit term acts as an effective magnetic field, described by eqn. 1.13, on an electron moving in an electric field. This Lorentz correction example is useful in illustrating how spin relaxation can occur, via spin-orbit coupling, in the absence of an applied magnetic field. The next section will discuss modeling the spin-orbit interaction, and thus spin relaxation, in a semiconducting solid, where band structure properties determine the final form of the spin-orbit term.

As an aside, the name *spin-orbit* derives from the case of spherical symmetry with a radial electric field, where  $\mathbf{E} = -\mathbf{r} \frac{1}{r} \frac{\partial V}{\partial r}$ . Since  $\mathbf{v} = \mathbf{p} \frac{1}{m}$ ,  $\mathbf{v} \times \mathbf{E}$  becomes  $\mathbf{L} \frac{1}{mr} \frac{\partial V}{\partial r}$ , and

$\boldsymbol{\sigma} \cdot \mathbf{L}$  ( $\boldsymbol{\sigma}$  represents spin and  $\mathbf{L}$  is orbital angular momentum) appears explicitly in the spin-orbit term.

### Spin relaxation in semiconductors

In semiconductors, spin-orbit coupling is determined largely by the symmetries of the crystal band structure. One source of spin-orbit coupling in semiconductors is bulk inversion asymmetry. Unlike Si and Ge, GaAs and other zinc-blende structure materials lack a center of inversion. In materials that lack bulk inversion symmetry, band states with different spin quantum numbers are nondegenerate, even in the absence of a magnetic field. Written symbolically,  $E_n(\mathbf{k}, \uparrow) \neq E_n(\mathbf{k}, \downarrow)$ . Splitting of energy states based on spin resembles the effect of a magnetic field, and hence, can be modeled by an effective magnetic field. The conduction band spin splitting in III-V materials, derived from bulk inversion asymmetry, was first described in 1955 by Dresselhaus [92] and the Hamiltonian can be written as:

$$\hat{H}_{Dresselhaus} = \gamma_D \sum_{i=x,y,z} \sigma_i k_i (k_{i+1}^2 - k_{i+2}^2), \quad (i+3 \rightarrow i) \quad (1.16)$$

where  $\gamma_D$  is the Dresselhaus coupling coefficient generally expressed in units of energy times length cubed (e.g. eV Å<sup>3</sup>) and  $k$  is the electron momentum component. Equation 1.16 has the form of  $\boldsymbol{\sigma} \cdot \mathbf{B}_{\text{eff}}$  with an effective magnetic field

$$\mathbf{B}_{\text{eff}, Dresselhaus} \propto \begin{pmatrix} k_x(k_y^2 - k_z^2) \\ k_y(k_z^2 - k_x^2) \\ k_z(k_x^2 - k_y^2) \end{pmatrix}. \quad (1.17)$$

Another source of spin-orbit coupling within a semiconductor is structural inversion asymmetry, where  $V(\mathbf{r}) \neq V(-\mathbf{r})$ . While traveling in a semiconductor, an electron feels a potential gradient ( $\nabla V$ ) that can exist from a variety of sources such

as an externally applied electric field, or internal fields derived from energy band bending in semiconductor device junctions and heterostructures. Since  $\mathbf{E} = -\nabla V$ , a moving electron will feel an effective magnetic field from the potential gradient described in a similar manner as that shown in the previous section with the Lorentz transformation. This source of spin-orbit coupling inside a semiconductor was first described in 1960 by Rashba [93] with the Hamiltonian:

$$\hat{H}_{Rashba} = \alpha_R \sum_{i=x,y,z} \sigma_i (k_{i+1} E_{i+2} - k_{i+2} E_{i+1}), \quad (i+3 \rightarrow i) \quad (1.18)$$

where  $\alpha_R$  is the Rashba coupling coefficient generally expressed in units of energy times length (e.g. eV Å). Here, the effective magnetic field has the form

$$\mathbf{B}_{\text{eff}, Rashba} \propto \mathbf{k} \times \mathbf{E} = \begin{pmatrix} k_y E_z - k_z E_y \\ k_z E_x - k_x E_z \\ k_x E_y - k_y E_x \end{pmatrix}. \quad (1.19)$$

Thus, the spin-orbit term can now be expressed as

$$\hat{H}_{so} = \hat{H}_{Dresselhaus} + \hat{H}_{Rashba} \quad (1.20)$$

where  $\hat{H}_{Dresselhaus}$  and  $\hat{H}_{Rashba}$  are given by equations 1.16 and 1.18, respectively. The main distinction between Rashba and Dresselhaus coupling is their dependence on the electron crystal momentum, where the Rashba term varies with  $k$ , while the Dresselhaus term varies with  $k^3$ .

An additional source of spin-orbit coupling can come from structural strain such as that from external stress on the structure or lattice mismatch in heterostructures. Although not discussed in detail here, strain can be modeled by a deformation potential described in terms of the unstrained potential, with an added correction dependent

on a strain tensor times a potential gradient. Again, the potential gradient in the deformation potential can act as an electric field with an effective magnetic field, and contributes to the Hamiltonian via Rashba coupling.

Calculating the effect of spin-orbit coupling from the Dresselhaus and Rashba terms can be simplified by assuming confinement in a particular plane. This assumption corresponds to, for example, quantum confinement provided by a quantum well structure. For a (100) quantum well sample, setting the [100]-direction as  $z$ , and the confinement plane as the  $xy$ -plane, results in  $k_z = 0$  and  $k_z^2 \rightarrow \langle k_z^2 \rangle$ , where  $\langle \rangle$  indicate an average or expectation value. Also, assuming that the confining potential ( $V$ ) is inversion symmetric in the  $xy$ -plane, then  $\frac{\partial V}{\partial x} = \frac{\partial V}{\partial y} = 0$  and  $\mathbf{E} = E_z \hat{z}$ . With these assumptions, the Dresselhaus and Rashba Hamiltonians become:

$$\hat{H}_{Dresselhaus} = \gamma_D [\sigma_x k_x k_y^2 - \sigma_y k_y k_x^2 - \langle k_z^2 \rangle (\sigma_x k_x - \sigma_y k_y)] \quad (1.21)$$

$$\hat{H}_{Rashba} = \alpha_R (\sigma_x k_y - \sigma_y k_x) \quad (1.22)$$

### 1.2.4 Spin Relaxation Mechanisms

This final introductory section summarizes the main spin relaxation mechanisms that are relevant to electron spins in semiconducting solids. Note that only electron spin relaxation is discussed, since theoretically, hole spins are expected to relax quickly relative to electron spins due to intermixing of heavy-hole and light-hole states in the valence band.<sup>1</sup> Empirically, longer spin lifetimes have been observed for electrons than for holes in semiconductor systems [28].

---

<sup>1</sup>Although a large split-off between the light and heavy holes can lead to longer hole spin lifetimes [94].

### **D'yakonov-Perel' Spin Relaxation**

The D'yakonov-Perel' (DP) spin relaxation mechanism derives from a  $k$ -dependent effective magnetic field that exists in materials that lack bulk inversion symmetry, and has been shown to be the most important spin relaxation mechanism in low doped GaAs systems [28,60]. The spins dephase as the effective magnetic field varies depending on the electron momentum. Theoretically, the DP spin relaxation rate is inversely proportional to the momentum scattering rate and also becomes more efficient ( $\sim E_{\mathbf{k}}^3$ ) at increasing electron energies for hot electrons. In addition, the DP mechanism is generally suppressed by a magnetic field applied along the direction of the spins, as the applied field competes with the effective magnetic field [28,60].

### **Elliot-Yafet Spin Relaxation**

Another spin relaxation mechanism is the Elliot-Yafet (EY) spin relaxation mechanism where spin-orbit coupling couples electron states of opposite spins and in combination with momentum scattering, leads to spin relaxation. The EY spin relaxation rate is directly proportional to momentum scattering and plays a significant role in small bandgap and large spin-orbit split materials [28]. The opposite dependence on momentum scattering distinguishes the DP and EY mechanisms, where the DP mechanism results in dephasing of spins in between collisions while the EY mechanism accounts for spin relaxation during collisions.

### **Bir-Aronov-Pikus Spin Relaxation**

A third spin relaxation mechanism is the Bir-Aronov-Pikus (BAP) mechanism, which derives from electron interaction with holes. Spin relaxation can occur via scattering with holes and the rate depends on several factors describing the type of hole in the interaction. In the nondegenerate case, the BAP spin relaxation rate is proportional

to the hole population, while it is proportional to the cube root of the hole population in the degenerate case [28, 60].

### **Hyperfine Interaction**

A final spin relaxation mechanism is the hyperfine interaction where electron spins can relax by interacting with the nuclear spins in the crystal solid. Although the GaAs nuclei carry a  $3/2$  spin, the hyperfine interaction is only significant for electrons in localized states such as quantum dots or dilute dopant levels. For spin injection, electrons are injected at energies above the bottom of the conduction band, and the effects from the hyperfine interaction are expected to be negligible.

## Chapter 2

# Spin Injector Fabrication and Spin Detection Techniques

This short chapter describes the experimental methods employed in the spin injection studies of this dissertation. The first part summarizes spin injector fabrication with magnetron sputtering. The second part of the chapter describes the optical detection technique and experimental setup used to measure the injected spin polarization inside the semiconductor.

### 2.1 Spin Injector Fabrication

All magnetic tunnel spin injectors were grown in an entirely self-contained custom designed magnetron sputtering deposition system, shown in fig. 2.1, at the IBM Almaden Research Center. Two types of spin injectors were grown for spin injection, a magnetic tunnel transistor (MTT) spin injector and a CoFe-MgO spin injector (see fig.2.2). The deposition process utilized shadow mask patterning, which provided fast, efficient production of tunnel injector junctions on semiconductor substrates. For the MTT spin injector, a rectangular ferromagnetic base layer was grown first, followed

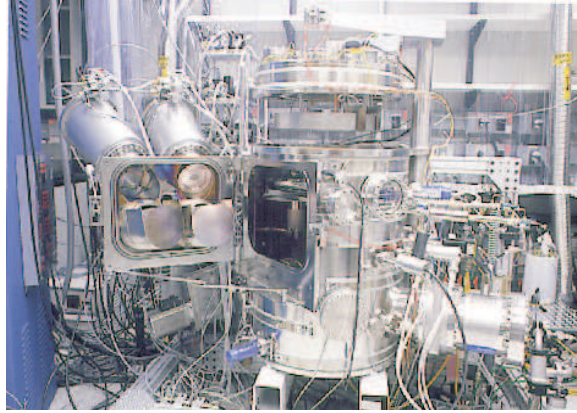


Figure 2.1: Photograph of the magnetron sputtering deposition system used to grow MTT and CoFe-MgO tunnel spin injectors.

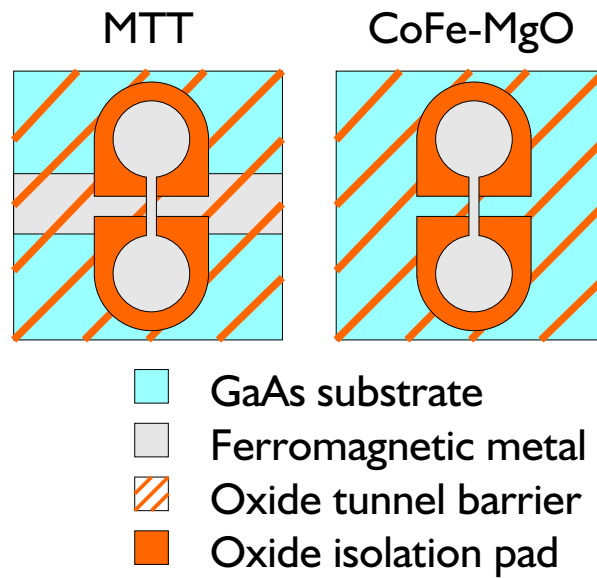


Figure 2.2: Top view drawing of the MTT and CoFe-MgO spin injectors.

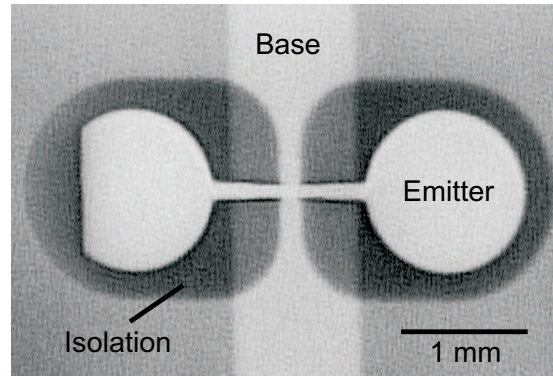


Figure 2.3: Top view photograph of a MTT.

by a thin  $\text{Al}_2\text{O}_3$  tunnel barrier grown over the entire sample. After deposition of the tunnel barrier, thick  $\text{Al}_2\text{O}_3$  isolation pads were deposited to prevent shorting of the emitter layer to the substrate. Finally, the ferromagnetic emitter layer was grown on top of the isolation pads, along with a Ta capping layer to prevent oxidation of the emitter. For the CoFe-MgO spin injector, a thin MgO(100) tunnel barrier was grown first over the entire sample, followed by the deposition of MgO isolation pads and a CoFe emitter layer capped with Ta. The isolation pads and emitter layers defined the junction area. The substrates for the spin injection structures consisted of GaAs based quantum well heterostructures that were used to optically detect the spin polarization of injected electrons. The substrates were grown by molecular beam epitaxy at Stanford University.

A top view of a real MTT device is shown in fig. 2.3 where the thin tunnel oxide is not visible. The CoFe-MgO junction looks similar to the MTT, only without the rectangular base ferromagnetic layer.

## 2.2 Optical Detection of Spin Polarization

The detection of spin polarization inside a semiconductor is nontrivial. The detectors used here are GaAs based quantum well light emitting diodes, which emit circularly polarized light corresponding to the electron spin polarization. With this technique, the electron spin polarization inside the quantum well can be measured directly.

### 2.2.1 Optical Selection Rules

The band structure of bulk GaAs around the  $\Gamma$  point is sketched in fig. 2.4. The conduction band states are *s*-like and have zero orbital angular momentum. Thus, the total angular momentum of electrons in the conduction band derives from spin only, and the band is two-fold degenerate for the two available spin states.<sup>1</sup> The valence band is *p*-like and has an orbital angular momentum of one. Thus, the total angular momentum of the hole states has both spin and orbital components. As shown in fig. 2.4, the valence band states have bands denoted the heavy-hole (HH), light-hole (LH), and split-off band. Spin-orbit interaction leads to the split-off band, where the energy of a given state is lower when the magnetic moment from a spin is aligned with the magnetic moment from the electron orbital angular momentum. The heavy-hole and light-hole states are degenerate at the  $\Gamma$  point in bulk GaAs, however in quantum wells, the degeneracy is lifted due to confinement (the two bands have different effective mass), and strain for materials such as InGaAs. Also, the heavy-hole band has a higher density of states near the  $\Gamma$  point because it has less dispersion than the light-hole band, leading to an approximately three times greater light emission from radiative electron-HH recombination than electron-LH recombination [60].

In the Faraday geometry, where the electron spin is aligned along the direction

---

<sup>1</sup>In actuality, for GaAs the degeneracy in the conduction band is lifted due to bulk inversion asymmetry. See section 1.2.3.

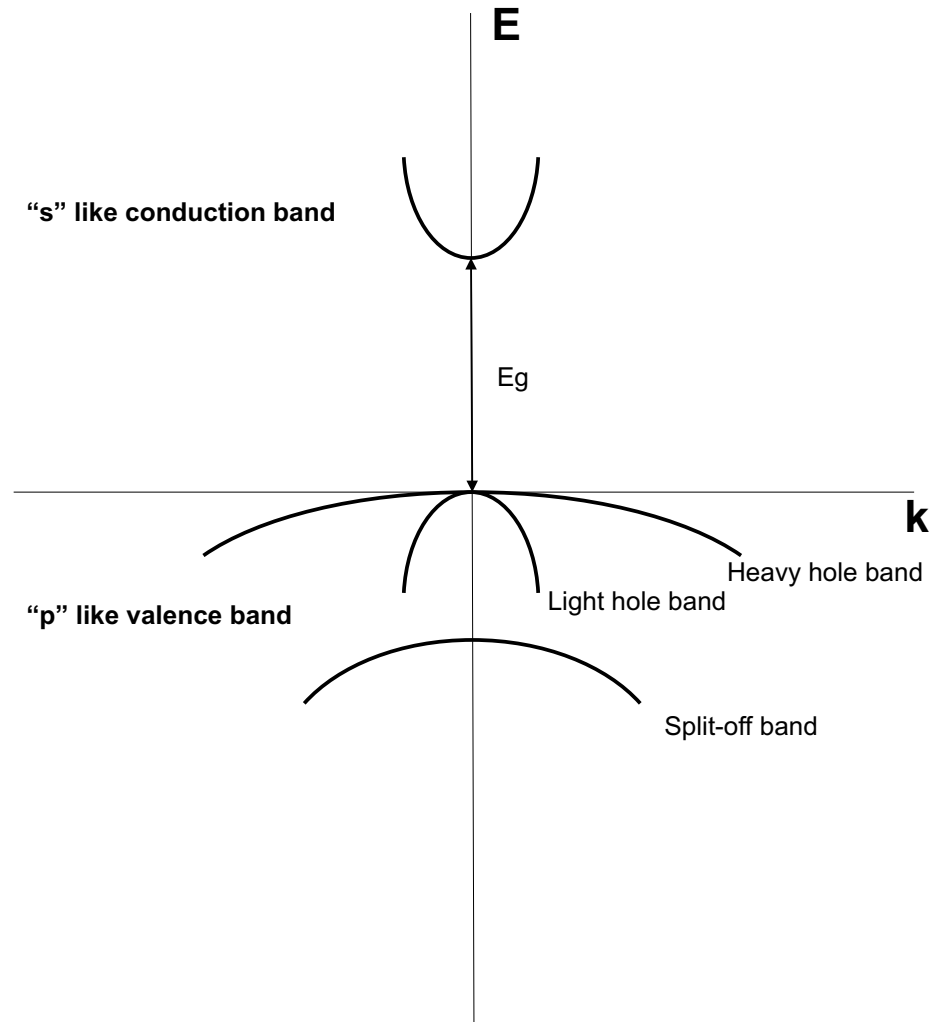


Figure 2.4: E vs. k band diagram for bulk GaAs around the  $\Gamma$  point.

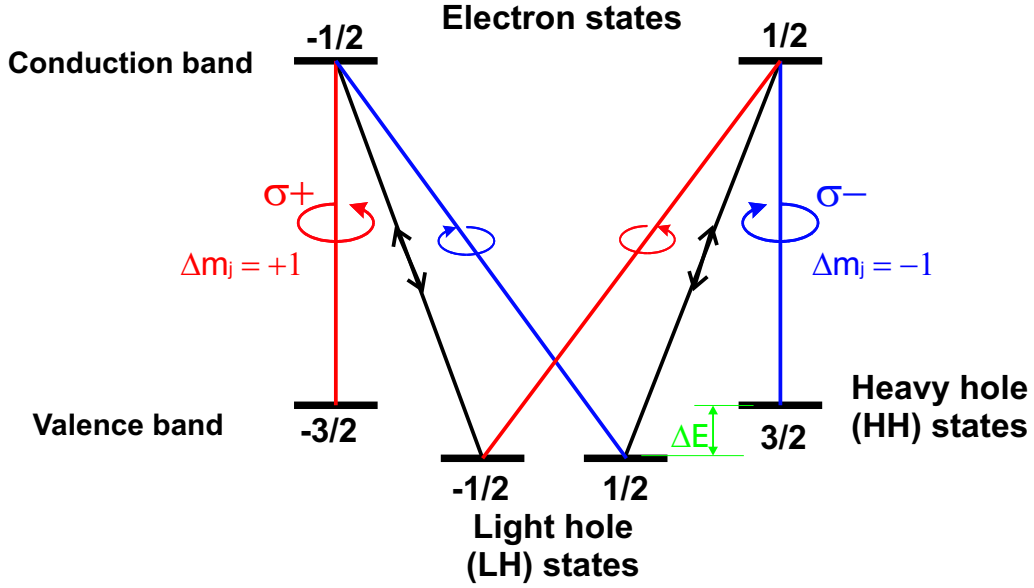


Figure 2.5: Optical recombination selection rules in the Faraday geometry.

of light propagation, radiative recombination in the quantum well follows well defined optical selection rules [60]. The selection rules are shown in fig. 2.5, where the electron and hole states are labeled by their total angular momentum quantum number. Circular polarized light can only transfer  $(\Delta m_j) \pm 1$  angular momentum to the system, and as shown in fig. 2.5, luminescence from the quantum well will have a circular polarization corresponding to the spin of the recombining electron [60, 95]. For electron-HH recombination, a  $-1/2$  electron will recombine with a  $-3/2$  hole state emitting  $\sigma^+$  circularly polarized light, while a  $+1/2$  electron will recombine with a  $+3/2$  hole state emitting  $\sigma^-$  circularly polarized light. The two light components are sometimes denoted as left-hand and right-hand circularly polarized for  $\sigma^+$  and  $\sigma^-$ , respectively. When one points the thumb along the light propagation direction, the curling of the fingers matches the rotating direction of the electric field vector belonging to the associated light component.

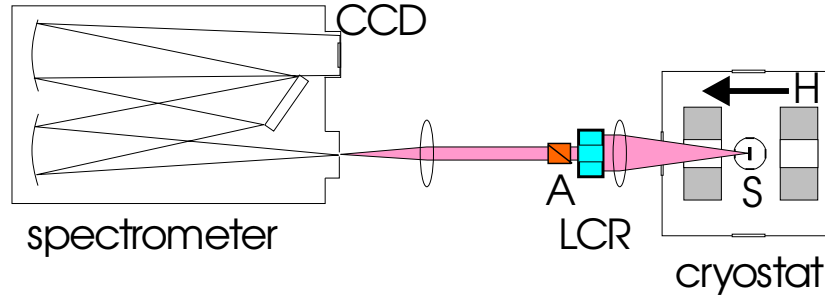


Figure 2.6: Experimental setup for optical studies of spin injection.

### 2.2.2 Optical Detection Setup

The experimental setup for the optical spin detection technique used in the spin injection experiments is illustrated in fig. 2.6.<sup>2</sup> The sample (S) sits inside a superconducting magnet cryostat, which allows temperature control from 1.4 to 300 K and also applies an external magnetic field of up to 7 T. The sample is oriented such that the applied magnetic field (H) is parallel to the propagation direction of the luminescence being measured, perpendicular to the sample film plane. Again, this geometry, where the applied magnetic field and the electrons spins are aligned along the axis of the propagation direction of the luminescence, is called a Faraday geometry. As described in the previous section, only in the Faraday geometry will the emitted light exhibit a circular polarization that is directly correlated with the spin of the recombining electrons. A liquid crystal retarder (LCR) in combination with a linear polarizer (A) analyzes the circularly polarized light components, with a selected component then being measured by a grating spectrometer and a charge-coupled device (CCD). Based on the circular polarization of the luminescence, the radiative recombination from electrons of both spin orientations can be counted separately, giving a direct measurement of the spin polarization inside the quantum well immediately before recombination.

<sup>2</sup>A separate experimental setup for time resolved optical studies is described in chapter 5.



# Chapter 3

## Magnetic Tunnel Transistor Spin Injector

This chapter presents the initial characterization of spin injection using the MTT as a spin injector into a GaAs-InGaAs quantum well heterostructure [96]. The  $\text{In}_{0.2}\text{Ga}_{0.8}\text{As}$  quantum wells in GaAs form a light emitting diode (LED) that emits circularly polarized light, where the strength of polarization is dependent on the spin orientation of the recombining electrons. Electroluminescence from the  $\text{In}_{0.2}\text{Ga}_{0.8}\text{As}$  quantum wells shows a polarization of  $\sim 10\%$  with MTT spin injection at 1.4 K after a linear background subtraction in the applied magnetic field. The electroluminescence polarization is found to be strongly dependent on the collector-to-base bias voltage across the semiconductor LED heterostructure.

### 3.1 Introduction

As noted previously (see section 1.2), creating a population of spin polarized electrons inside a semiconductor is an initial step towards developing spin-based electronic devices. The MTT (see section 1.1.4) represents a potential candidate for spin injection

that is not affected by the conductivity mismatch problem [79] of diffusive contacts since electrons are injected ballistically into the semiconductor collector [90]. In addition, contrary to spin injectors with a single FM layer, the MTT is not limited by the spin dependent Fermi level tunneling spin polarization of the FM metal [48, 49, 53]. Instead, the spin polarization of injected electrons is determined by spin filtering in the base region where the polarization can approach 100% [55, 57]. Another advantage of the MTT is that it offers more degrees of freedom for transport manipulation. With three terminals, both the emitter-to-base and collector-to-base bias voltages can be controlled to manipulate the spin polarized injection current. While the MTT can potentially provide a highly spin polarized injection current, a significant shortcoming is the relatively low collector current as most of the current passes through the base contact.

For this spin injection study, the collector of the MTT structure is a GaAs-InGaAs quantum well heterostructure that allows for optical detection of the injected electron spins. The overall MTT spin injector structure is illustrated in the band diagram schematic in fig. 3.1.

## 3.2 MTT-Spin LED Fabrication

The semiconductor spin detector LED was grown by molecular beam epitaxy (MBE). Starting with a beryllium doped  $p$ -GaAs substrate, three  $p$ -Al<sub>0.32</sub>Ga<sub>0.68</sub>As layers (total thickness of 780 nm) with stepped doping concentrations were grown followed by a 60 nm Al<sub>0.32</sub>Ga<sub>0.68</sub>As intrinsic layer. The AlGaAs layers help confine injected electrons to the quantum wells and also prevent beryllium dopant diffusion into the quantum wells. Next, three GaAs-In<sub>0.2</sub>Ga<sub>0.8</sub>As quantum wells were grown on top of the AlGaAs layers, with InGaAs well widths of 8 nm and GaAs well spacing widths of 15 nm. On top of the quantum wells, an additional 5 nm Al<sub>0.32</sub>Ga<sub>0.68</sub>As layer was

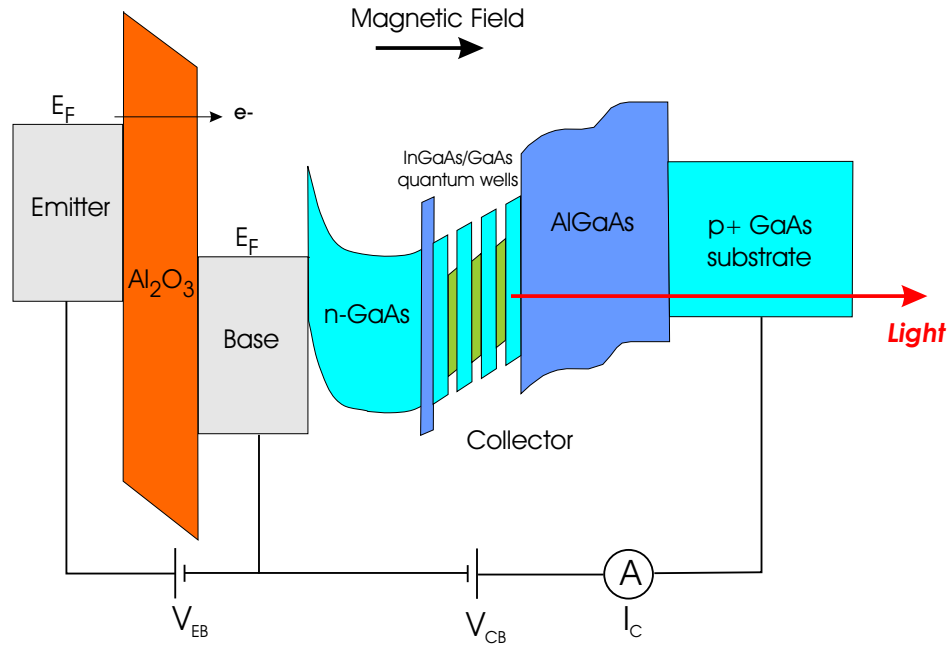


Figure 3.1: Band diagram of an MTT on a GaAs-InGaAs spin detector LED.

added to help confine holes traveling from the  $p$ -type back-side to the quantum well region for recombination. Finally, 100 nm of  $n$ -GaAs, with a doping concentration  $\sim 5 \times 10^{16} \text{ cm}^{-3}$ , forms the top layer of the GaAs collector. The top GaAs layer was lightly doped to reduce current leakage due to Schottky tunneling from the eventual base layer. Before removal from the MBE chamber, an arsenic cap layer was deposited on top of the GaAs to protect the surface layer from oxidation after removal from the MBE chamber.

After growing the semiconductor collector structure, the sample was placed inside a high vacuum sputtering chamber and heated to  $\sim 520 \text{ }^\circ\text{C}$  to remove the arsenic cap by sublimation. After cooling to ambient temperature, a MTJ was then grown on top of the GaAs, to form the MTT, using DC magnetron sputtering with shadow mask patterning. Three masks patterned the base, emitter isolation, and emitter layers, respectively [53]. The base layer consists of 3.5 nm Ni<sub>81</sub>Fe<sub>19</sub> deposited directly on the

GaAs, followed by a second layer of 1.5 nm  $\text{Co}_{84}\text{Fe}_{16}$ . A thin ( $\sim 1.5 \text{ \AA}$ ) aluminum layer was then deposited to prevent oxidation of the underlying base layer. Next, an aluminum oxide ( $\text{Al}_2\text{O}_3$ ) tunnel barrier was grown via reactive sputtering of aluminum metal in an oxygen ambient. The final oxide thickness was  $\sim 2.2 \text{ nm}$ . Then after deposition of the isolation pads, 5 nm of  $\text{Co}_{84}\text{Fe}_{16}$  was deposited for the emitter layer and then capped with 5 nm of Ta to prevent emitter oxidation.

There are several advantages to using GaAs-InGaAs quantum wells. First, the InGaAs quantum well luminescence energy is smaller than the bandgap of GaAs, which allows back-side measurement of the electroluminescence signal. Measuring the signal through the GaAs substrate, as opposed to front-side emission, minimizes the effect of magnetic circular dichroism derived from polarization dependent interaction between the luminescence and the FM layers. Second, the heavy-hole (HH) and light-hole (LH) energy splitting ( $\Delta E$  in fig. 2.5) in InGaAs, due to confinement and strain, is greater than either emission linewidth. Photoluminescence studies on the 8 nm wide  $\text{In}_{0.2}\text{Ga}_{0.8}\text{As}$  quantum wells indicate a  $\sim 40 \text{ nm}$  wavelength separation between electron-HH and electron-LH emission peaks. As shown in the next section, the emission linewidth of the electroluminescence signal is  $\sim 3 \text{ nm}$ . Thus, the electron-HH recombination emission can be analyzed independently without any contribution from electron-LH emission, which emits distinctly different circularly polarized light for a given spin population (see fig. 2.5).

Figure 3.1 shows the bias voltage setup and approximate band effects of the entire device structure. The emitter-to-base bias ( $V_{EB}$ ) controls the energy of the tunneling electrons while the collector-to-base bias ( $V_{CB}$ ) controls the band bending of the semiconductor LED structure. The magnetic field is applied perpendicular to the film plane, along the axis of the light propagation for detection, consistent with a Faraday geometry. Note, the direction of the applied field is determined by the requirement of the Faraday geometry in the optical detection scheme, and therefore,

large fields are required to rotate the FM magnetic moments out of the film plane.

The applied magnetic field creates a spin asymmetry in the MTT injector proportional to the net magnetic moments of the FM layers. The emitter injects spin polarized electrons into the base, where the electrons undergo spin dependent scattering determined by the magnetic orientation of the base layer. The electrons with spin parallel to the majority spin of the base layer are scattered to a lesser degree than those with an antiparallel spin. Here, the external field aligns the emitter and base layer moments. Only electrons that retain sufficient energy to overcome the Schottky barrier at the base collector interface are collected as current. As a result, minority spin electrons from the emitter layer are removed preferentially from the current, and the net current injected into GaAs should be highly spin polarized. The injected electrons then relax energetically into the quantum wells and recombine with unpolarized holes from the substrate, emitting light with a circular polarization corresponding to the spin of the recombining electrons.

### 3.3 Electroluminescence Spectra and Polarization

Electroluminescence measurements at 1.4 K with  $V_{EB} = -2.06$  V and  $V_{CB} = 1.0$  V are shown in fig. 3.2. The electroluminescence signal is dependent on the applied magnetic field, where  $\sigma^+$  circularly polarized emission dominates in positive fields,  $\sigma^-$  circularly polarized emission dominates in negative fields, and the two components are identical in zero field.<sup>1</sup> Figure 3.3 shows the energy splitting of spin states under positive applied magnetic field. The relative energy of an electron spin state under

---

<sup>1</sup> $\sigma^+$  and  $\sigma^-$  emissions are defined in section 2.2.1.

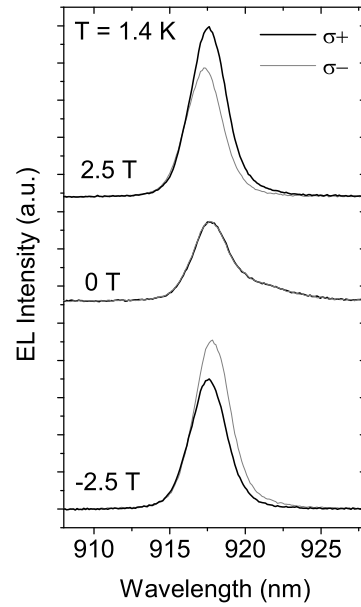


Figure 3.2: Electroluminescence intensity vs. wavelength at 1.4 K for applied magnetic fields of 2.5, 0, and -2.5 T with  $V_{EB} = -2.06$  V and  $V_{CB} = 1.0$  V. Dark and light lines represent  $\sigma^+$  (left-hand) and  $\sigma^-$  (right-hand) circularly polarized light, respectively.

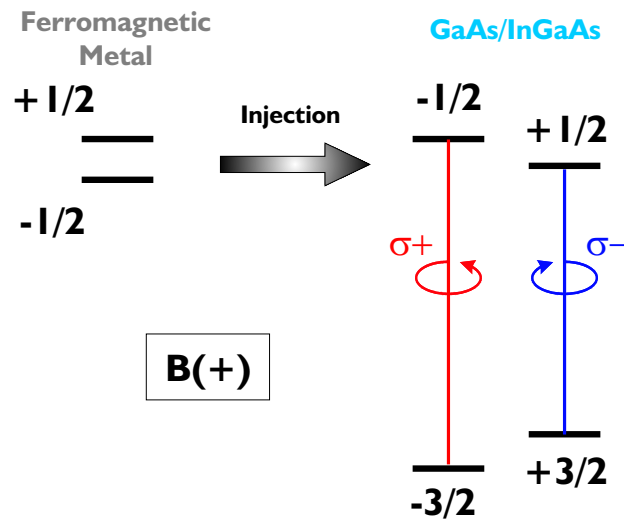


Figure 3.3: Schematic energy representation of spin states under positive magnetic field based on the Zeeman equation (eqn. 3.1).

an external field is determined by the Zeeman equation:

$$E_{Zeeman} = -\mathbf{m} \cdot \mathbf{B} \quad (3.1)$$

$$\mathbf{m} = -g\mu_B m_s$$

where  $\mathbf{m}$  is the magnetic moment of the electron,  $\mathbf{B}$  is the magnetic flux density,  $g$  is the material  $g$ -factor,  $\mu_B$  is the Bohr magneton, and  $m_s$  is the spin quantum number with a value of  $\pm\frac{1}{2}$ . Under a positive magnetic field, the  $-\frac{1}{2}$  electron spin state is the majority spin state in the FM metal, while GaAs and InGaAs have a negative  $g$ -factor and thus have a spin state energy splitting opposite to that in the FM metal. The injected  $-\frac{1}{2}$  spin electrons recombine and emit  $\sigma^+$  luminescence. Since this representation of spin injection and recombination matches that shown in fig. 3.2 with  $\sigma^+$  ( $\sigma^-$ ) dominating at positive (negative) field, the electroluminescence signal indicates majority carrier injection. This point is worth noting since the primary purpose of the spin injector is to create a large population of majority spin carriers for spin polarized current.

For analyzing the electroluminescence signal shown in fig. 3.2, the emission intensity for each polarization component is measured for a range of applied magnetic fields, and then their integrated intensities are used in the following equation to determine the circular polarization of the electroluminescence (EL):

$$P_{EL} = \frac{I^+ - I^-}{I^+ + I^-} \quad (3.2)$$

where  $I^+$  and  $I^-$  are the integrated intensities of the  $\sigma^+$  and  $\sigma^-$  components, respectively. Again, the optical selection rules within the quantum well under Faraday geometry correlate the circular polarization of the emitted light to the spin polarization of electrons immediately prior to recombination [60, 95].

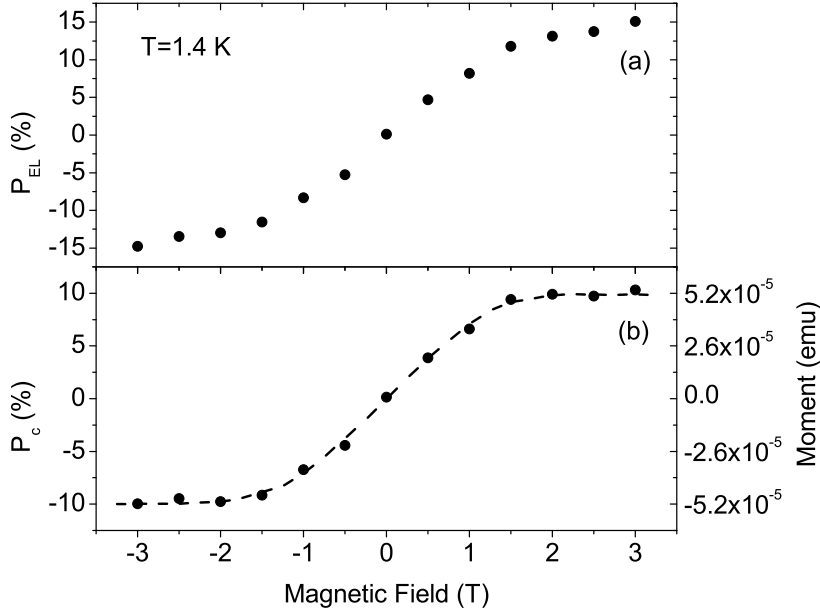


Figure 3.4: Electroluminescence polarization at 1.4 K (a) measured data and (b) after subtraction of a linear background. Bias voltage conditions are the same as in fig. 3.2. Dashed line in (b) represents the net magnetic moment of the MTT injector measured with a SQUID magnetometer at 10 K.

### 3.4 Polarization Dependence on Magnetic Field

Figure 3.4(a) shows the electroluminescence polarization ( $P_{EL}$ ) dependence on applied magnetic field at 1.4 K with  $V_{EB} = -2.06$  V and  $V_{CB} = 1.00$  V. The  $P_{EL}$  magnitude increases rapidly with magnetic field up to approximately  $\pm 2$  T, as the field rotates the magnetic moments of the emitter and base layers out of plane. The net magnetic moment of the MTT saturates out of plane at  $\sim 2$  T. Interestingly, there is an additional slow increase of  $P_{EL}$  at higher fields. Due to the negative  $g$ -factor of GaAs, low temperature thermalization of electrons should produce a background signal that decreases with magnetic field. One possible explanation for the positive background signal is that the light and heavy-hole splitting from the strain in the quantum wells is large enough that the hole spins no longer relax quickly compared

to the electrons. Normally, the wave function intermixing of the hole states results in extremely fast hole spin relaxation. However, if the holes retain their spin, low temperature thermalization due to Zeeman splitting for the hole states, which have a larger  $g$ -factor than electrons, could lead to a positive background signal with increasing magnetic field.

A linear background subtraction is employed to remove the magnetic field dependent background contribution and yields a corrected polarization ( $P_C$ ) plot shown in fig. 3.4(b), which reveals a saturation polarization of  $\sim 10\%$ . Note that polarization dependent reflection at the FM base-GaAs interface may add artificially to the electroluminescence polarization. However, a separate photoluminescence experiment, where linearly polarized light is reflected off the base layer through the substrate, found this effect to show a polarization of less than 1% that was not field dependent. Finally, the dashed curve in fig. 3.4 represents the net magnetic moment of the MTT injector measured in a magnetic field, applied perpendicular to the film plane, with a superconductor quantum interference device (SQUID) at 10 K. The magnetic field dependence of the magnetization shows excellent agreement with the field dependence of  $P_C$ , where the net magnetic moment saturates at the same point as the measured electroluminescence polarization. This result confirms that  $P_C$  derives from the injection of spin polarized electrons from the MTT spin injector.

The saturated polarization of  $\sim 10\%$  obtained in fig. 3.4(b) corresponds to a minimum estimate of injected spin polarization into GaAs. The spin splitting in the GaAs conduction band from bulk inversion asymmetry is proportional to  $E^{\frac{3}{2}}$ , where  $E$  is the hot electron energy. Consequently, the D'yakonov-Perel' (DP) spin relaxation mechanism becomes more efficient at elevated electron energies [60]. The injected electrons likely lose a significant amount of spin polarization via the DP mechanism as they relax energetically to the bottom of the GaAs conduction band. Additional spin relaxation can also occur inside the quantum well before recombination [97, 98].

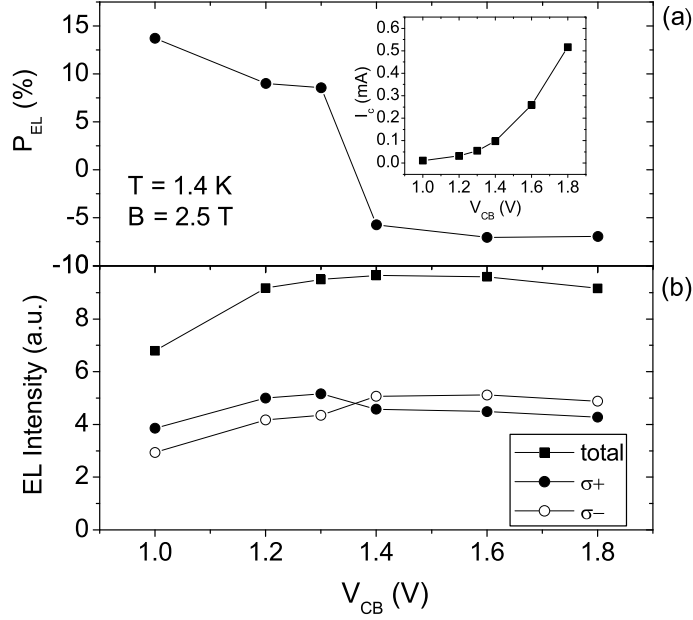


Figure 3.5: The collector-to-base bias voltage dependence of (a)  $P_{EL}$ , hole current (inset), and (b) electroluminescence intensity at 1.4 K and 2.5 T.  $V_{EB} = -2.06$  V for these measurements.

Thus, the actual injected spin polarization of electrons should be significantly higher than the measured electroluminescence polarization.

### 3.5 Polarization Dependence on Collector-Base Bias

Figure 3.5(a) summarizes the  $P_{EL}$  bias dependence on the collector-to-base voltage ( $V_{CB}$ ) at 1.4 K and an applied magnetic field of 2.5 T. For  $V_{CB} < 1$  V, the luminescence signal is too weak to obtain a  $P_{EL}$  value. Increasing  $V_{CB}$  above 1 V decreases  $P_{EL}$ , which changes sign at  $V_{CB} \sim 1.4$  V, and then settles at a relatively constant value with bias voltage. Note that  $P_{EL}$  does not exclude background effects. The sign reversal suggests that the injected electrons likely lose their initial spin orientation through spin relaxation, and then develop a polarization of the opposite spin orientation due

to thermalization to the  $+\frac{1}{2}$  spin state in the magnetic field in GaAs-InGaAs (see fig. 3.3) before recombination.

Increasing  $V_{CB}$  increases the hole current flowing from the  $p$ -GaAs substrate. Elevated electron-hole interactions can result in a higher spin relaxation rate through the Bir-Aronov-Pikus (BAP) mechanism [60]. With a low hole concentration, the spin relaxation rate is proportional to the number of holes in the quantum wells, and thus the relaxation rate increases with increasing bias voltage. However, above a threshold hole concentration, in the degenerate case, the BAP mechanism exhibits a much smaller dependence on the hole population [60]. Other spin relaxation processes could also show a bias voltage dependence. For example, the DP mechanism is very sensitive to hot electron energy, becoming much more efficient at higher energies [60]. Higher biases bend the conduction band of the  $n$ -GaAs region lower in energy, increasing the amount of energy relaxation needed for hot electrons to reach the bottom of the quantum wells to recombine. This increased energy relaxation process likely elevates the loss of electron spin orientation.

The bias dependence of electroluminescence intensity at 2.5 T appears in fig. 3.5(b). Initially, electron-hole recombination becomes more efficient with increasing bias, as more holes are injected into the quantum wells to recombine with electrons. However, the intensity saturates with bias near 1.4 V (approximately the turn-on voltage for the diode), as the signal becomes limited by the number of injected electrons from the MTT and stays relatively constant. Meanwhile, the intensity of the  $\sigma^+$  component decreases significantly, likely because spin relaxation becomes more efficient at high biases and electrons also thermalize to the  $+\frac{1}{2}$  state before recombination. As a result,  $P_{EL}$  becomes negative.

## 3.6 Summary

The magnetic tunnel transistor has successfully demonstrated spin injection into GaAs, measured directly using electroluminescence, and has the potential for applications in future spin-based research and device development. The MTT has the advantage of utilizing a base layer for spin filtering and could provide electron currents approaching 100% spin polarization. In addition, the three terminals allow for extended study and manipulation of the electrical transport characteristics. Unfortunately, the tunneling process along with the spin filtering and transport over the Schottky barrier interface results in very small injected current levels, which limit the electroluminescence signal used to measure the injected spin polarization. Indeed, the low luminescence signals prevented further studies examining the spin injection dependencies on emitter-to-base bias and temperature. Based on magnetocurrent transport measurements, higher injected polarizations are expected at lower emitter-to-base bias voltages. While the initial results using optical detection infer only modest values of spin polarized current, these values are more likely limited by spin relaxation mechanisms inside the semiconductor rather than the MTT injector. The measured 10% polarization is therefore a lower bound value for the injected spin polarization.

# Chapter 4

## CoFe-MgO(100) Tunnel Spin Injector

Addressing the experimental obstacles of the MTT injector, this chapter reports the higher injected electron spin polarization achieved with a CoFe-MgO tunnel injector into an AlGaAs-GaAs quantum well spin detector [99, 100]. The spin polarization is measured directly using optical detection of the electroluminescence signal emitted from an  $\text{Al}_x\text{Ga}_{1-x}\text{As}$ -GaAs quantum well. Spin injection from CoFe-MgO tunnel injectors creates electroluminescence polarizations exceeding  $\sim 50\%$  at 100 K and exceeding  $\sim 30\%$  at 290 K inside GaAs. The tunnel injectors also demonstrate excellent thermal stability, retaining efficient spin injection even after exposures to temperatures up to 400 °C. Finally, the electroluminescence polarization is found to exhibit a strong bias voltage dependence and, interestingly, a dramatic nonmonotonic dependence on temperature.

## 4.1 Introduction

Spin injection, as discussed previously in section 1.2.2, is an important area of research for the development of spin-based devices. Within spintronics technology, magnesium oxide (MgO) will likely play a key role in a variety of applications. While the MTT can enhance injector spin polarization through spin filtering of hot electrons in the base region, another possible approach for highly spin polarized electron injection is to exploit MgO as a spin filtering tunnel barrier.

Amorphous aluminum oxide ( $\text{Al}_2\text{O}_3$ ) is universally popular as the tunnel barrier in magnetic tunneling devices because it is robust and comparatively easy to grow uniformly without pinholes. Unfortunately, theoretical analysis of tunneling transport remains difficult for these devices due to the amorphous nature of the barrier. In addition, a clear epitaxial relationship between  $\text{Al}_2\text{O}_3$  and FM metals does not exist [24]. On the other hand, crystalline MgO as a tunnel barrier allows for theoretical modeling and prediction of spin polarized tunneling. Optimistic calculations predict a TMR ratio in excess of 1000% for a MgO(100) barrier of  $\sim 20$  atomic planes coinciding with a majority electron dominant spin polarized current [23].

Theoretical modeling by Butler et al. [24] predicts that tunneling conductance through crystalline MgO(100) is determined by the symmetry between Bloch states in the FM metal and the evanescent states inside the tunnel barrier. The majority spin tunneling conductance involves electrons in the Bloch state with  $\Delta_1$  symmetry where the transverse momentum is small ( $k_{\perp} \sim 0$ ), and which decays slowly across the tunnel barrier. Minority tunnel conductance is primarily through interface resonance states. This picture favors majority carrier spin polarized tunneling through an MgO barrier [24, 25].

Experimental studies with magnetic tunnel junctions support the theoretical predictions of enhanced spin transport across MgO tunnel barriers. Yuasa et al. [101]

have reported 180% TMR at room temperature in single-crystal (100) Fe|MgO|Fe tunnel junctions. Parkin et al. [102] have reported an even higher  $\sim 220\%$  room temperature TMR in polycrystalline, but highly (100) textured, CoFe|MgO|CoFe tunnel junctions, while also measuring  $\sim 85\%$  tunneling spin polarization (TSP) in CoFe|MgO|AlSi tunnel structures using superconducting tunneling spectroscopy. This TSP value approaches values observed from half-metallic ferromagnets [103].

The results obtained with MgO tunnel barriers exceed the typical values of traditional Al<sub>2</sub>O<sub>3</sub> MTJs, which display  $\sim 55\%$  TSP [15, 26], and room temperature TMR up to  $\sim 70\%$  [104]. Both the theoretical predictions and the experimental data from MgO-based tunneling structures suggest that MgO could be utilized in highly efficient tunnel spin injectors.

## 4.2 Injector-Spin LED Fabrication

A band diagram schematic of the CoFe-MgO spin injector grown on an AlGaAs-GaAs quantum well structure appears in fig. 4.1. Figure 4.2 shows a cross-section transmission electron micrograph (XTEM) of the spin injector and detector structure. The individual layers are readily distinguishable and the MgO and CoFe layers, although polycrystalline, are highly (100) textured.

The semiconductor spin LED detector, with a single GaAs quantum well, was grown by molecular beam epitaxy (MBE). The full semiconductor structure was:  $p$ -GaAs substrate | 570 nm  $p$ -Al<sub>*x*</sub>Ga<sub>1-*x*</sub>As | 75 nm  $i$ -Al<sub>*x*</sub>Ga<sub>1-*x*</sub>As | 10 nm  $i$ -GaAs | 15 nm  $i$ -Al<sub>*x*</sub>Ga<sub>1-*x*</sub>As | 100 nm  $n$ - or  $p$ -Al<sub>*x*</sub>Ga<sub>1-*x*</sub>As | 5 nm  $i$ -GaAs. Different aluminum concentrations ( $x$ ) were used to vary the quantum well depth. Doping of the top AlGaAs layer was varied to be either  $n \sim 5 \times 10^{16} \text{cm}^{-3}$  or  $p \sim 1 \times 10^{17} \text{cm}^{-3}$ . The final GaAs top layer protects the AlGaAs layer from oxidation in subsequent processing. The semiconductor samples were then capped with an arsenic layer to

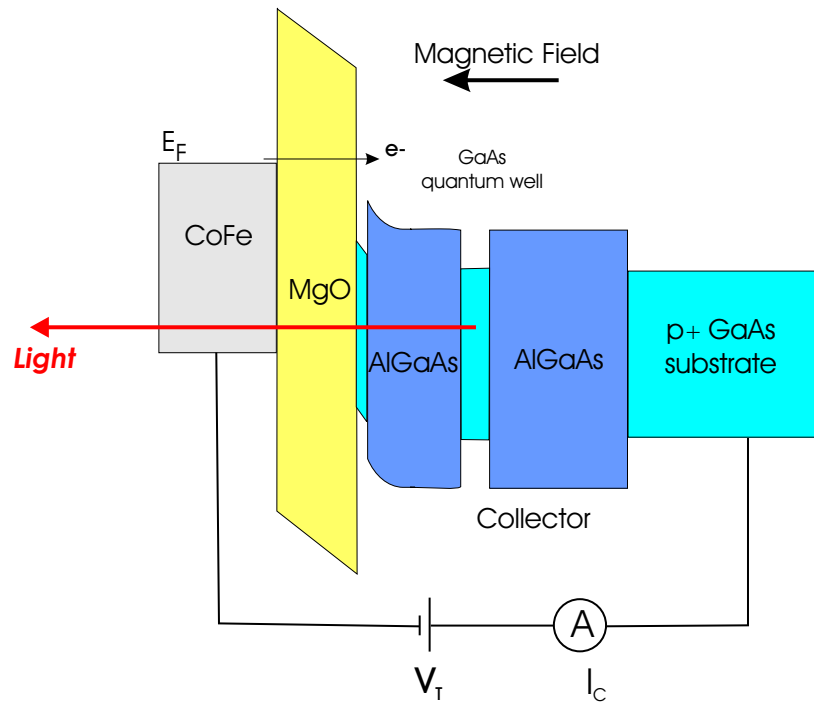


Figure 4.1: Band diagram of a CoFe-MgO spin injector grown on an AlGaAs-GaAs spin LED structure.

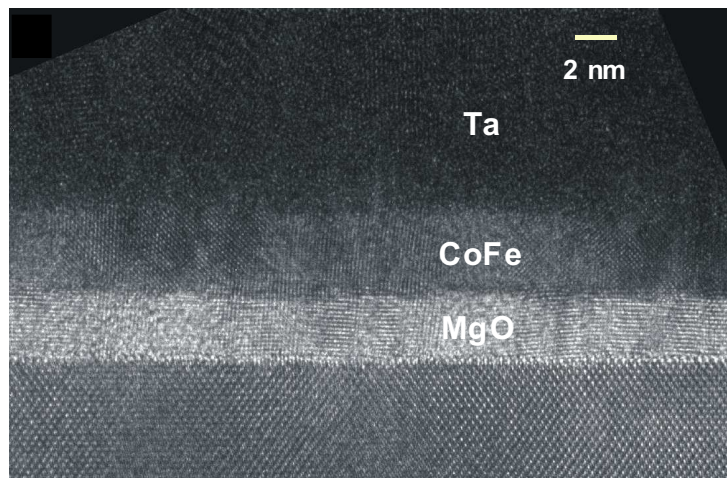


Figure 4.2: XTEM image of a CoFe-MgO spin injector sputter deposited on GaAs.

prevent damage during transport from the MBE chamber to the magnetron sputtering system, where the tunnel spin injectors were grown. Before deposition of the injector, the samples were heated to 550 °C for 10 minutes to remove the arsenic cap. After cooling to ambient temperature, a shadow mask deposition process was utilized to define the tunnel barrier ( $\sim 3$  nm MgO) and top FM electrode (5 nm  $\text{Co}_{70}\text{Fe}_{30}$  capped with 5-10 nm Ta to prevent oxidation). The final active injector area was  $\sim 100 \times 300 \mu\text{m}^2$ . A single voltage source ( $V_T$ ) controlled the bias voltage across the entire injector-semiconductor structure (see fig. 4.1).

The tunnel injector-spin LED structure grown here addresses several issues that complicated the previous MTT injector study. First, with a smaller  $g$ -factor ( $\sim -0.44$ ), a GaAs quantum well introduces a lower magnetic field dependent background polarization than an InGaAs quantum well.<sup>1</sup> Second, a single quantum well simplifies the quantum well structure. Disadvantages compared to InGaAs include the smaller light and heavy-hole band splitting and the need to measure the luminescence from the front-side of the sample. Although the electron-LH emission peaks are closer to the electron-HH emission peaks in this setup (relative to the InGaAs quantum well), the spectra nevertheless do not overlap and remain distinct. Back-side emission from the GaAs quantum well is largely reabsorbed by the GaAs substrate, and therefore front-side emission is used to measure the injected polarization. Light traveling through the spin injector will lose intensity and also acquire a background polarization signal, due to circular dichroism, from interaction with the FM metal. However, the direct injection of electrons into the semiconductor results in a sufficient electroluminescence signal, while background effects from interaction with the FM metal are small compared to the final measured polarizations. The tunnel injector is more robust than the MTT injector as the MTT can have (or develop) a poor Schottky barrier

---

<sup>1</sup>InAs has a  $g$ -factor of  $\sim -20$ , while the  $g$ -factor for InGaAs falls in between the values for GaAs and InAs

or emitter-base tunnel barrier. The metal-insulator-semiconductor structure setup allows for a voltage distribution that will not easily break the tunnel barrier. Finally, the two layer CoFe-MgO tunnel spin injector is easier to grow than the MTT.

Figure 4.1 illustrates the direction of light propagation and also the direction of magnetic field, which again must be applied perpendicular to the film plane in order to obtain the required Faraday geometry of the detection scheme. The magnetic field rotates the CoFe magnetic moment out of the film plane, creating an asymmetry of electron spins aligned perpendicular to the film. This spin polarized population is then injected directly into the AlGaAs-GaAs heterostructure where they relax energetically and recombine in the GaAs quantum well, emitting circularly polarized light corresponding to the spin polarization of electrons injected into the quantum well.

## 4.3 CoFe-MgO on an Al<sub>0.08</sub>Ga<sub>0.92</sub>As-GaAs quantum well heterostructure

### 4.3.1 Electroluminescence Measurements

Sample electroluminescence spectra are shown in fig. 4.3 for an *n-i-p* sample structure with 8% Al doped barriers with applied magnetic fields of 5, 0, and -5 T at 100 K. Note that the electron-LH peaks appear in fig. 4.3. These peaks are absent in the emission spectra from the GaAs-InGaAs quantum wells in fig. 3.2, where the compressive strain in the InGaAs splits off the light-hole band from the heavy-hole band significantly. While there is minimal strain in the AlGaAs-GaAs quantum wells, the split off between the light and heavy-hole bands due to confinement is sufficient to allow unambiguous analysis of electron-HH emission only. The electron-HH emission

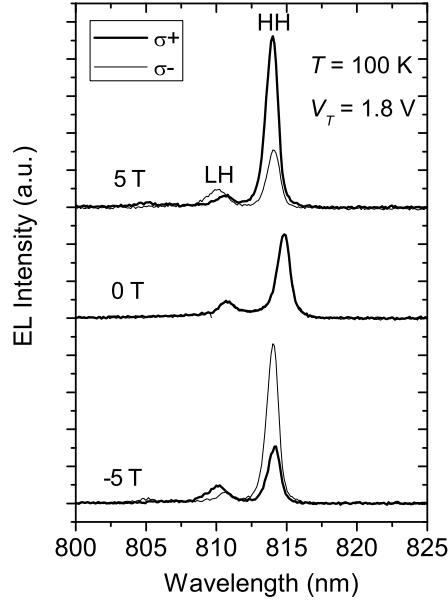


Figure 4.3: Electroluminescence intensity vs. wavelength for an  $n$ - $i$ - $p$  8% Al doped barrier sample at 100 K for applied magnetic fields of 5, 0, and -5 T with  $V_T = 1.8$  V. Dark and light lines represent  $\sigma^+$  (left-hand) and  $\sigma^-$  (right-hand) circularly polarized light, respectively.

indicates majority carrier injection (see section 3.3) where  $\sigma^+$  ( $\sigma^-$ ) emission dominates at positive (negative) magnetic field. As expected, neither circularly polarized component dominates in the absence of a magnetic field indicating that at zero field, there is no net spin polarization of electrons perpendicular to the film plane. Also note that in fig. 4.3, the emission peaks shift to higher energy (lower wavelength) and the intensity increases significantly in the magnetic field. The shift to higher energy is normally attributed to the diamagnetic shift as materials naturally oppose applied magnetic fields [105]. Experimentally, the enhancement of the luminescence in a magnetic field is consistent with a shorter radiative recombination lifetime, which would contribute to a positive magnetic field dependent background polarization as spins would have less time to relax before recombining radiatively with holes.

The polarization of the electroluminescence signal is determined using eqn. 3.2

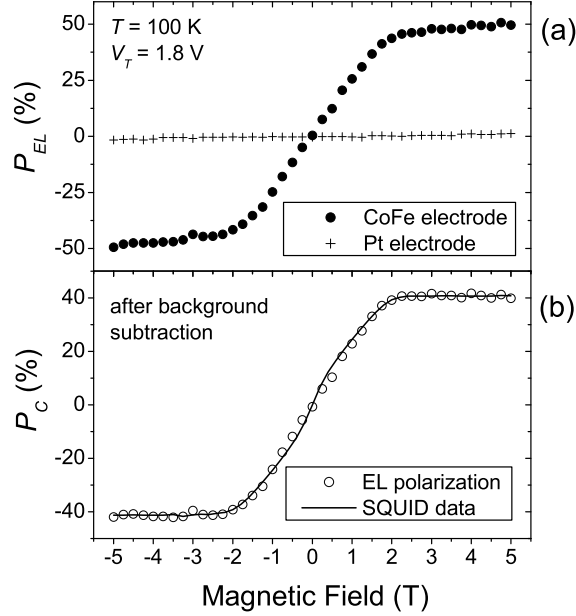


Figure 4.4: Electroluminescence polarization vs. magnetic field at 100 K for a CoFe-MgO spin injector grown on an 8% Al barrier,  $n$ - $i$ - $p$  spin LED sample (a) before and (b) after background polarization subtraction. A comparative measurement for a nonmagnetic Pt injector is shown in (a) and a SQUID magnetometer measurement of the CoFe magnetic moment overlays the background corrected data in (b).

restated here for convenience:

$$P_{EL} = \frac{I^+ - I^-}{I^+ + I^-}$$

where  $I^+$  ( $I^-$ ) is the integrated electron-HH  $\sigma^+$  ( $\sigma^-$ ) emission intensity. Note that, as expected, the electron-LH emission has an opposite polarization as compared to the electron-HH emission, consistent with the optical selection rules described in section 2.2.1. Recall that the electroluminescence polarization represents a lower bound value for the injected polarization as it measures the spin polarization of the electrons immediately before radiative recombination [60,95]. Due to spin relaxation, the injected electron spin polarization will be reduced during the lifetime within the semiconductor before recombination.

Figure 4.4(a) shows the electroluminescence polarization dependence on applied magnetic field for an 8% Al doped barrier, *n-i-p* sample at 100 K. The polarization increases rapidly with magnetic field magnitude up to  $\sim 2$  T, as the field rotates the CoFe moment out of the film plane. Above 2 T,  $P_{EL}$  continues to increase linearly, although at a slower rate, and reaches  $\sim 50\%$  at 5 T. The linear increase of  $P_{EL}$  after saturation of the CoFe magnetic moment could derive from a combination of a suppression of spin relaxation by the magnetic field and a shorter radiative recombination lifetime in the magnetic field, as discussed earlier. Indeed, a longitudinal magnetic field (in this case, perpendicular to the film plane) reduces D'yakonov-Perel' (DP) spin relaxation [60], which is generally considered the most important spin relaxation mechanism in our experiment (see section 1.2.4). Note, control photoluminescence measurements conducted on similar quantum well structures using circularly polarized pump light also show a decreased spin relaxation in the presence of a longitudinal magnetic field.

A magnetic field dependent recombination lifetime can also contribute to the background signal. The stronger luminescence intensities at higher magnetic fields suggest a shorter radiative recombination lifetime. This effect can lead to an increasing polarization with increasing field as carriers have less time to spin relax before being measured optically. Note that the Zeeman splitting in GaAs is negligible compared to thermal energies at 100 K and, therefore, cannot account for the observed background polarization.

The electroluminescence polarization corrected ( $P_C$ ) by subtracting a linear, magnetic field dependent, background polarization is shown in fig. 4.4(b). Ideally, this corrected polarization represents a measure of spin polarization excluding the influence of the external magnetic field on spin relaxation and recombination lifetime, and is measured as high as 42% at 100 K. The solid line in fig. 4.4(b) is the CoFe magnetic moment measured in a perpendicular-to-plane magnetic field with a SQUID

magnetometer at 20 K. The normalized field dependence of the electroluminescence polarization shows excellent agreement with the SQUID data, which is consistent with the electroluminescence polarization being a result of the injection of spin polarized electrons from the CoFe layer.

As a reference measurement, the  $P_{EL}$  of a control sample with a nonmagnetic Pt electrode in place of CoFe is also shown in fig. 4.4(a). The polarization is on the order of 1% and has a very weak magnetic field dependence. Additional photoluminescence experiments with linearly polarized pump light, both reflected and transmitted through the CoFe layer, also gave small polarizations ( $< 2\%$ ) and a weak field dependence. These results indicate that the effects of polarization-dependent light absorption or reflection by the metal and semiconductor layers are very small.

### 4.3.2 Bias Voltage and Temperature Effects

The bias voltage dependence of  $P_C$  over a 1.4-100 K temperature range is summarized in fig. 4.5 for both  $n-i-p$  and  $p-i-p$  samples with 8% Al doped barriers. The relatively small confinement potential of the GaAs-Al<sub>0.08</sub>Ga<sub>0.92</sub>As quantum well results in weak electroluminescence signals at elevated temperatures, and becomes a limiting factor for measurements above 100 K. Over the available temperature range,  $P_C$  decreases with bias at any given temperature.

A similar bias dependence in photoluminescence experiments has been attributed to spin relaxation through the DP mechanism before photoexcited electrons recombine in the quantum wells [106, 107]. Recall that DP spin relaxation occurs in semiconductors lacking bulk inversion symmetry due to spin precession about an effective magnetic field, whose orientation and magnitude depend on the electron's momentum. A higher bias voltage results in a larger effective magnetic field and consequently, more rapid spin relaxation.

A notable point is the lack of data at lower biases in fig. 4.5. Returning to the

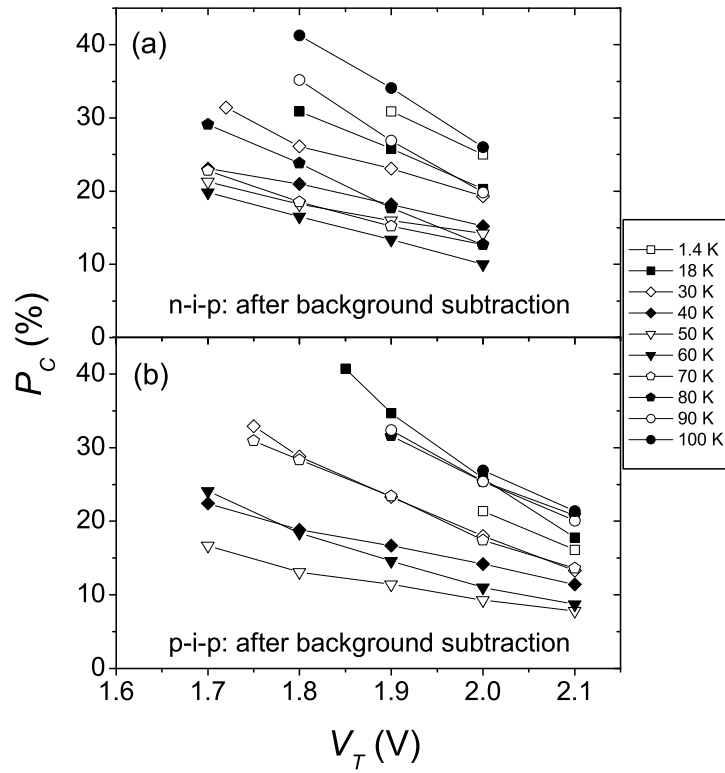


Figure 4.5:  $P_C$  vs. bias voltage over a 1.4-100 K temperature range for (a)  $n-i-p$  and (b)  $p-i-p$  samples with 8% Al doped barriers.

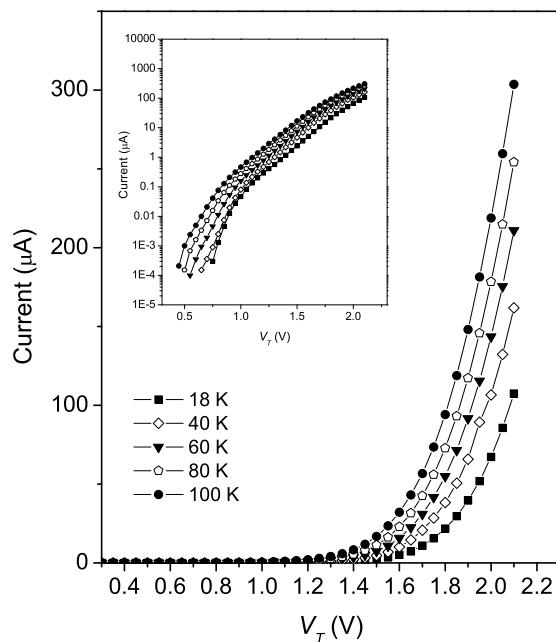


Figure 4.6: Current-voltage characteristics for an 8% Al  $n-i-p$  sample. The data was taken at 0 T. Data at 5 T was nearly identical. Inset is the same data, plotted on a log scale for reference.

band diagram schematic in fig. 4.1, a sufficient signal-to-noise ratio in the electroluminescence signal is obtained only after the overall device turn-on. The applied bias must first turn-on the semiconductor junction.<sup>2</sup> Then mobile holes from the substrate move to the MgO-GaAs interface, allowing biasing of the tunnel barrier for spin injection. The current-voltage plot in fig. 4.6 for an 8% Al barrier  $n-i-p$  sample illustrates the bias voltage needed to turn on the overall spin injector-semiconductor structure.

Perhaps more intriguing is the nonmonotonic temperature dependence of  $P_C$ , which has a high value at low temperatures and at first, decreases with temperature towards a minimum at  $\sim 50 - 60$  K.  $P_C$  then increases with temperature up to

<sup>2</sup>The heavily doped  $p$ -type substrate makes a  $p-i-p$  band structure qualitatively similar to an  $n-i-p$  band structure for the low surface doping concentrations in the spin detectors.

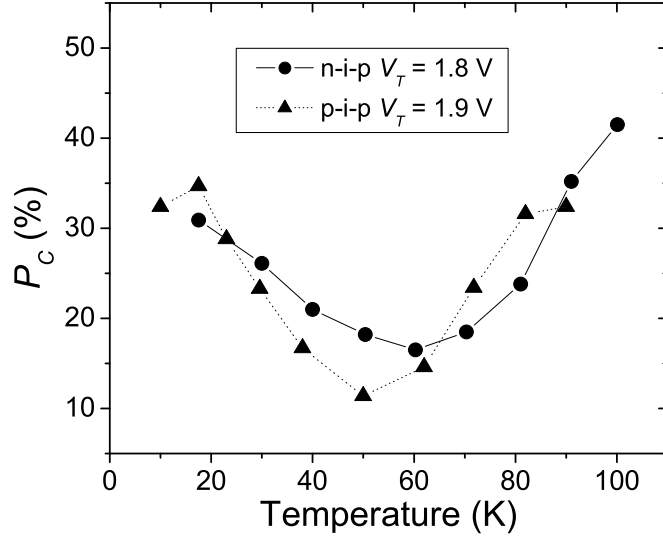


Figure 4.7:  $P_C$  vs. temperature for both  $n-i-p$  (circles) and  $p-i-p$  (triangles) samples with 8% Al doped barriers at a given bias voltage.

100 K, the highest temperature at which measurements could be made with the 8% Al doped barrier quantum wells. Figure 4.7 illustrates this unique temperature dependence more clearly, plotting  $P_C$  at a given bias voltage as a function of temperature for both  $n-i-p$  and  $p-i-p$  samples.

The nonmonotonic temperature dependence can be explained by the temperature dependencies of both carrier recombination lifetime and spin relaxation, and is the focus of the study presented in chapter 5. In short, recombination lifetime is important as the longer the lifetime, the longer the electron has to relax in spin before being measured or removed from the system through a nonradiative pathway. For spin relaxation, the DP spin relaxation rate is given by [108]:

$$\frac{1}{\tau_s^{DP}} \propto \tau_p \cdot T, \quad (4.1)$$

and is proportional to the momentum scattering time ( $\tau_p$ ) because frequent electron

momentum scattering randomizes the orientation of the effective internal magnetic field from which the DP mechanism is derived. From eqn. 4.1, the DP spin relaxation rate follows a temperature dependence similar to carrier mobility. Ionized impurity scattering, which has a weak temperature dependence, dominates momentum scattering at low temperatures and the DP spin relaxation rate increases with temperature. At high temperatures polar optical phonon scattering, which increases rapidly with temperature, dominates the momentum scattering and the DP spin relaxation rate decreases with temperature.

The contribution of other spin relaxation mechanisms, such as the Elliot-Yafet (EY) and Bir-Aronov-Pikus (BAP) mechanisms, could be important if the DP relaxation rate is low. However, EY or BAP spin relaxation cannot explain the non-monotonic nature of the  $P_C$  temperature dependence. The EY spin relaxation rate is proportional to the momentum scattering rate and thus would have the opposite temperature dependence as our experimental data, while the BAP relaxation, due to electron-hole exchange interactions, displays a monotonic temperature dependence.

Note that magnetic field effects are also important in our experiment. As stated earlier, the radiative recombination lifetime shows a magnetic field dependence (see section 4.3.1), which could contribute to the background slope seen above the  $\sim 2$  T saturation value. The background signal also varies with temperature. Figure 4.8 compares the polarization measured in a 5 T field to the background corrected  $P_C$ . A negative background signal appears below  $\sim 40$  K, likely due to thermalization in the Zeeman split carrier states and the negative  $g$ -factor of GaAs. This effect diminishes as the temperature increases since thermal energies become larger than the Zeeman splitting energy. The background slope signal then becomes positive at higher temperatures, likely due to magnetic field suppression of DP spin relaxation and reduction of the radiative recombination lifetime in the magnetic field. Due to

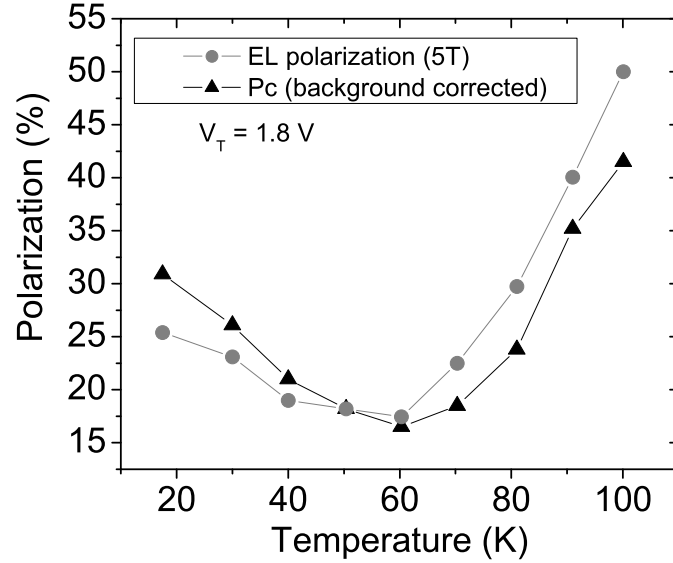


Figure 4.8: Measured electroluminescence polarization at 5 T (circles) and background corrected  $P_C$  (triangles) vs. temperature for an 8% Al  $n$ - $i$ - $p$  sample at  $V_T = 1.8$  V.

the temperature dependence of the background signal, the background corrected polarization  $P_C$  provides a means to compare an effective zero field electroluminescence polarization at different temperatures. However, the linear subtraction method likely oversimplifies the background contribution and could lead to temperature dependent artifacts.

A final point to note is the applied bias voltage,  $V_T$ , across the entire spin injector-semiconductor structure. As the temperature changes, the total voltage drop across the MgO barrier, the  $n$ - or  $p$ -AlGaAs depletion region, and the quantum well region can vary slightly even when  $V_T$  remains constant. As shown in fig. 4.5,  $P_C$  is sensitive to the bias conditions and raises the question that the temperature dependence of  $P_C$  may derive from variations in the bias voltage distribution across the entire structure. However, varying the voltage drops across different regions of the

spin injector-semiconductor structure would introduce a monotonic temperature dependence, and therefore cannot account for the experimental results. In addition, current-voltage characteristics, shown in fig. 4.6, do not reveal any anomalies that would result in the observed temperature dependence.

### 4.3.3 Thermal Annealing and Stability

After the initial polarization measurements, the samples were then annealed in a high vacuum anneal furnace at various temperatures in an effort to obtain higher levels of spin injection analogous to the post anneal improvements seen in the TMR of MTJs and the tunneling spin polarization of CoFe-MgO-AlSi tunnel structures [102]. Thermal annealing likely improves the crystal structure of the MgO and may also allow oxygen to diffuse out of the magnetic layers into the MgO, improving the tunneling interface. Figure 4.9 shows a  $\sim 10\%$  improvement in the measured electroluminescence polarization in an 8% Al *n-i-p* sample after annealing, with  $P_C$  reaching nearly 55% after the 340 °C anneal. Interestingly, the sample showed very little improvement for annealing temperatures up to 300 °C, and then a temperature dependent polarization improvement after annealing above 300 °C. Figure 4.10 shows a plot of  $P_C$  vs. temperature measured in the sample after annealing at sequentially higher temperatures. While  $P_C$  improved in general at all temperatures with annealing, the increase in polarization was significantly larger for temperatures greater than 70 K than for lower temperatures. Again, since MgO is crystalline, thermal annealing will likely improve the tunnel barrier quality as well as the MgO interfaces with both CoFe and GaAs if oxygen preferentially diffuses into the MgO. While these effects can explain the general improvement in spin injection, they cannot account for the unusual temperature dependent improvement in polarization observed in fig. 4.10.

One possible explanation for the temperature dependent improvement is a contribution from a low Curie temperature component to the magnetization of the device.

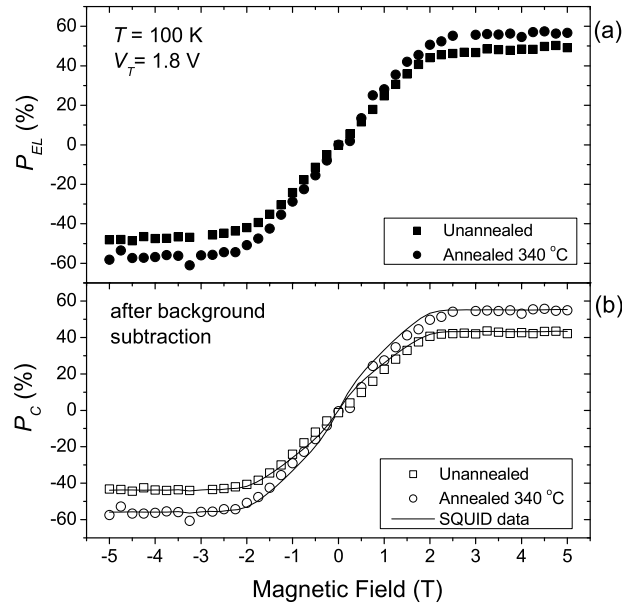


Figure 4.9: Improvement in electroluminescence polarization with thermal annealing for an 8% Al barrier  $n$ - $i$ - $p$  sample (a) before and (b) after background polarization subtraction. Data shown at 100 K and  $V_T = 1.8$  V.

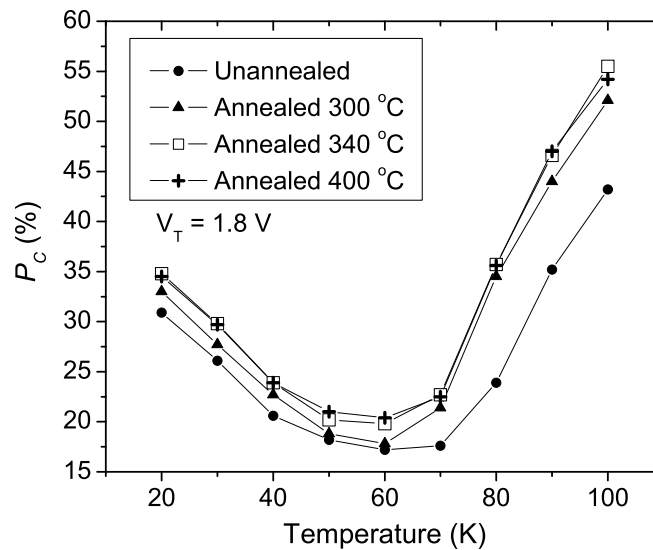


Figure 4.10:  $P_C$  vs. temperature for an 8% Al  $n$ - $i$ - $p$  sample after annealing at various temperatures up to 400 °C. Relatively greater polarization improvement is found for temperatures greater than  $\sim 70$  K.

Such a contribution is sometimes seen in MTJs with  $\text{Al}_2\text{O}_3$  barriers and may account for the large increase of TMR with decreasing temperature below  $\sim 70$  K [109]. Annealing could raise the Curie temperature of this component and thus extend its magnetization contribution to higher temperatures. However, the change in the polarization improvement seen between 70 K and 80 K is too abrupt to model as a Curie temperature effect. In any case, the origin of such an effect is unclear.

Another possible explanation for the experimental results are variations in the spin relaxation rate arising indirectly from thermal annealing. While the heterostructure is unlikely changed by the low (relative to MBE growth) temperature anneal treatments, changes in the tunnel barrier could affect the trajectories of the electrons injected into the semiconductor collector. The tunneling probability is exponentially dependent on the tunnel barrier thickness, thus, changes to the tunnel barrier structure could alter the angular spread of the cone of injected electrons. This effect could well result in changes in the spin relaxation rate, which is strongly dependent on the electron momentum perpendicular and parallel to the plane of the quantum well structure. Since the spin relaxation rate has a temperature dependence, such changes could result in a temperature dependent polarization improvement with annealing.

Overall the CoFe-MgO spin injectors show general improvement in the measured electroluminescence polarization at all temperatures after thermal annealing. While the temperature dependent improvement is intriguing, the most important aspect of fig. 4.10 is that the injected polarization remains at a high value, even after exposing the spin injectors to  $400^\circ\text{C}$ . This result demonstrates the excellent thermal stability of the CoFe-MgO spin injector, another desirable trait for the fabrication and processing aspects of a universal spin injector.

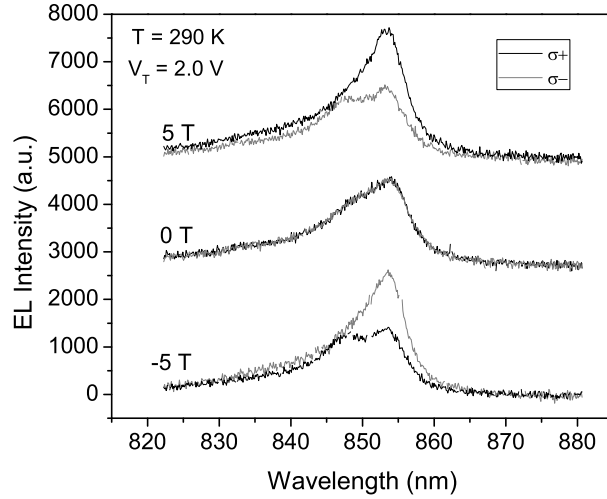


Figure 4.11: Electroluminescence intensity vs. wavelength for a 16% Al  $p$ - $i$ - $p$  sample at 290 K for applied magnetic fields of 5, 0, and -5 T with  $V_T = 2.0$  V.

## 4.4 CoFe-MgO on an $Al_{0.16}Ga_{0.84}As$ -GaAs quantum well heterostructure<sup>3</sup>

### 4.4.1 Electroluminescence Measurements

The 8% Al doped barrier quantum well samples discussed previously are unable to produce a significant electroluminescence signal above 100 K. Therefore, in order to obtain higher temperature results, 16% Al doped barriers are used to provide a larger energy confinement for carriers in the GaAs quantum well. For these samples, the electron-LH and electron-HH emissions are easily separable at low temperatures, but as shown for a 16% Al  $p$ - $i$ - $p$  sample in fig. 4.11, the emission peaks are much broader and overlap at room temperature. In this case, the emission peaks are fitted with Lorentzian functions, and the integrated electron-HH emission intensity is used in determining the electroluminescence polarization (eqn. 3.2). Again,  $\sigma^+$  ( $\sigma^-$ ) emission

<sup>3</sup>Samples described in this section have been annealed at 300°C for one hour.

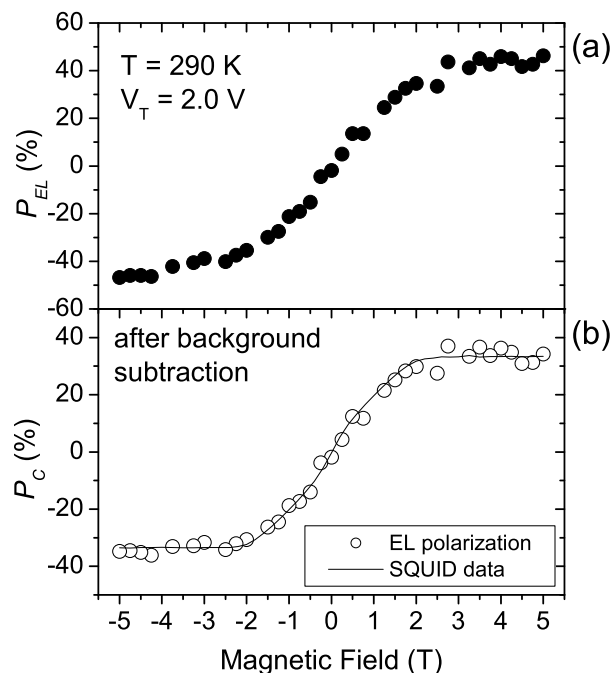


Figure 4.12: Electroluminescence polarization vs. magnetic field for a 16% Al *p-i-p* sample at 290 K with  $V_T = 2.0$  V, (a) before background and (b) after background polarization subtraction.

dominates at positive (negative) magnetic field for the electron-HH peak, and the two components are equal at 0 T. The spectra clearly indicate spin injection into the quantum well at 290 K. Note that the total intensity is much lower than that seen at low temperatures, as nonradiative pathways, such as carrier escape from the quantum well, become more significant at high temperatures. Also, the longer wavelength of the peaks is due to bandgap shrinking in GaAs with temperature.

Figure 4.12 shows the electroluminescence polarization measurement for a CoFe-MgO injector grown on a 16% Al barrier *p-i-p* spin detector at 290 K with  $V_T = 2.0$  V. Here, the CoFe-MgO tunnel spin injector demonstrates an injected spin polarization of nearly 50% in a 5T field and a background corrected polarization exceeding 30% at 290 K. Although the background signal is significant at high temperatures, the

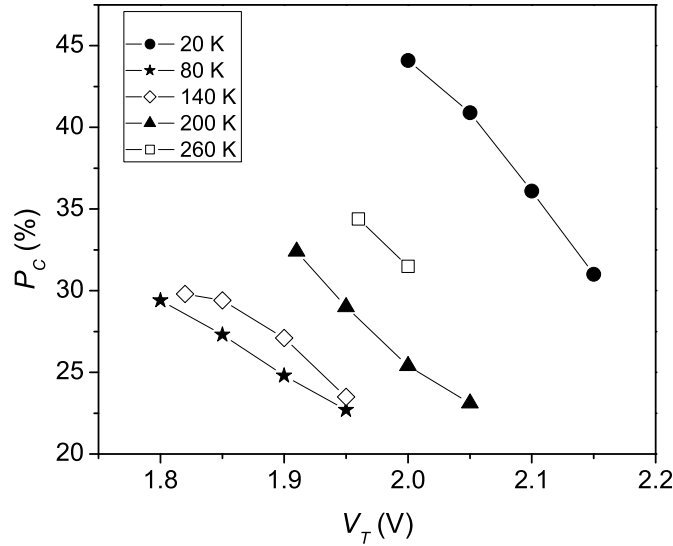


Figure 4.13:  $P_C$  vs. bias voltage at selected temperatures for a 16% Al  $p$ - $i$ - $p$  sample.

data after background subtraction ( $P_C$ ) still matches the SQUID data corresponding to the CoFe magnetic moment.

#### 4.4.2 Bias Voltage and Temperature Effects

Figure 4.13 shows the bias voltage dependence of  $P_C$  in a 16% Al  $p$ - $i$ - $p$  sample. Similar to the data from the samples with an 8% Al doped barrier quantum well,  $P_C$  decreases with increasing bias at all temperatures.

The temperature dependence of the electroluminescence polarization from 1.4-290 K is presented in fig. 4.14, which shows both the polarization at 5 T and the corrected  $P_C$  value. The  $P_C$  temperature dependence follows a similar nonmonotonic trend as that seen with the shallow 8% Al barrier quantum wells, although the rise in polarization at higher temperatures is less dramatic. Also, the values for  $P_C$  are lower than the values measured with shallow wells. This result is expected because the efficiency of the DP spin relaxation mechanism increases rapidly with electron

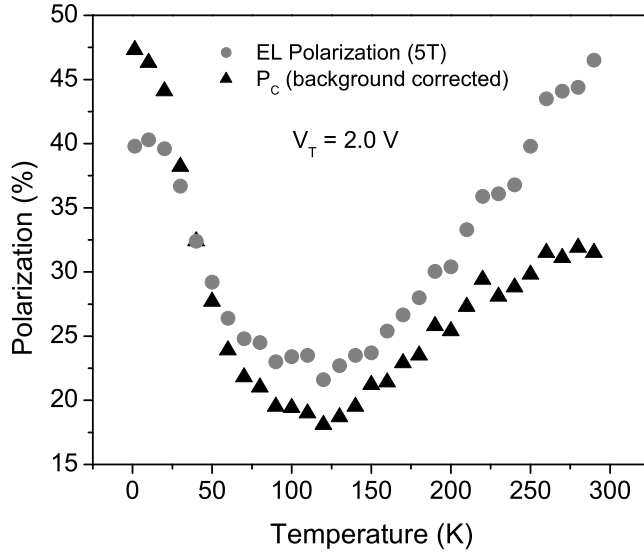


Figure 4.14: Measured electroluminescence polarization at 5 T (circles) and background corrected  $P_C$  (triangles) vs. temperature at  $V_T = 2.0$  V for a 16% Al  $p-i-p$  sample.

energy [60]. Hot electrons high in the conduction band will undergo significant spin relaxation during thermalization down to the bottom of the quantum well.

The 5 T data in fig. 4.14, as compared to  $P_C$ , reveals a strong temperature dependence of the background signal. A plot of the background signal with temperature is shown in fig. 4.15. At low temperatures, the background signal is negative, likely due to thermalization in the Zeeman split electron states inside GaAs, which has a negative  $g$ -factor. As the temperature increases, thermal energies become larger than the Zeeman splitting energy, diminishing this effect. The background then settles at a low positive value, which can be attributed magnetic field suppression of DP spin relaxation [60] and also to the field dependence of the recombination lifetime. Again, the total electroluminescence intensity at high fields is, in general, larger than that at low fields. This apparent field dependence of radiative recombination lifetime could be the source of the sharp increase in the background signal at high temperatures.

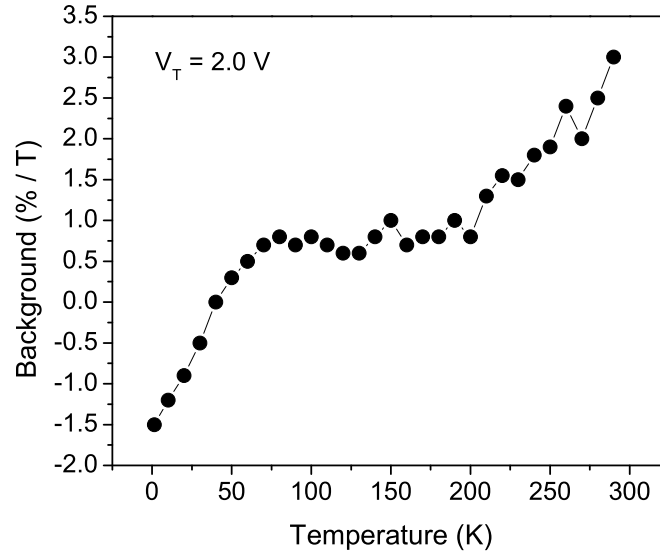


Figure 4.15: Background polarization signal vs. temperature for a 16% Al  $p$ - $i$ - $p$  sample with  $V_T = 2.0 \text{ V}$ .

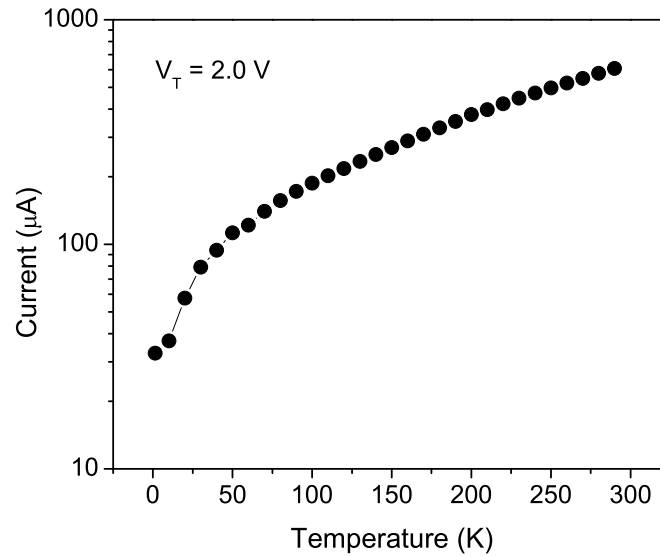


Figure 4.16: Current vs. temperature in a 16% Al  $p$ - $i$ - $p$  sample with  $V_T = 2.0 \text{ V}$ .

Overall, the bias voltage dependence and the temperature dependence of  $P_C$  display trends and behaviors similar to that observed in the shallow 8% Al quantum wells. A final note is that over the large temperature range from 1.4 K to 290 K, the current in the structure changes dramatically with increased thermal energy. However, no features were observed in the variation of electrical current with temperature, shown in fig. 4.16, that could account for the nonmonotonic temperature dependence of  $P_C$  or the background signal.

## 4.5 Summary

The CoFe-MgO spin injector, inspired by theoretical and experimental results showing high tunneling spin polarization in MgO-based tunneling structures, achieves several important goals of spin injection. First and foremost, it has demonstrated high levels of spin injection, exceeding 50% lower bound spin polarization at 100 K, and exceeding 30% lower bound spin polarization at 290 K measured in the electroluminescence polarization from GaAs quantum wells. Note, the high magnetic fields to rotate the CoFe moment out of the film plane are not fundamental, but a requirement of the optical detection scheme. For potential applications that do not require optical detection in the Faraday geometry, much smaller, or even zero, fields can be used to magnetize the CoFe along its easy axis. The CoFe-MgO spin injectors demonstrate excellent thermal stability, maintaining efficient spin injection after exposure to temperatures up to 400 °C. As with the MTT spin injector, the CoFe-MgO tunnel spin injector is grown by magnetron sputtering, a deposition technique capable of a high throughput of devices.

The stability and robustness of the CoFe-MgO injector on the AlGaAs-GaAs heterostructure allows for extensive studies of both the bias voltage dependence and the

temperature dependence of the injected spin polarization. These studies reveal a significant dependence of the electroluminescence polarization on both spin relaxation and the carrier recombination within the quantum well.



## Chapter 5

# Spin and Recombination Lifetime Effects in GaAs

While the CoFe-MgO tunnel spin injector achieves most of the goals for spin injection into semiconductors, an ideal spin injector would demonstrate a constant spin injection efficiency over a wide temperature range. In this chapter, the source of the nonmonotonic temperature dependence seen in the electroluminescence polarization from the GaAs quantum wells is investigated. The results from electrical spin injection are compared to an expected polarization value derived from time resolved optical measurements of carrier spin and recombination lifetime [110]. Time resolved optical studies suggest that the nonmonotonic temperature dependence seen in the electroluminescence polarization derives from a peak in the carrier recombination lifetime with temperature. These results provide evidence of temperature independent spin injection of  $\sim 70\%$  from 10 K to room temperature from the CoFe-MgO spin injectors.

## 5.1 Introduction

The temporal decay of both spin polarization and carrier population within a quantum well is expected to be exponential. Assuming a single exponential in each case, the optically measured polarization from the quantum well detector is related to the injected spin polarization by the following [111]:

$$P_{measured} = P_{injected} \cdot \frac{\tau_s}{\tau_s + \tau_r} = P_{injected} \cdot \left[1 + \frac{\tau_r}{\tau_s}\right]^{-1} \quad (5.1)$$

where  $\tau_s$  is the spin lifetime and  $\tau_r$  is the total carrier recombination lifetime defined by radiative ( $\tau_{rad}$ ) and nonradiative components ( $\tau_{nrad}$ ):

$$\tau_r^{-1} = \tau_{rad}^{-1} + \tau_{nrad}^{-1}. \quad (5.2)$$

As described by eqn. 5.1, the injected spin polarization of electrons will be reduced by a factor dependent on both the spin lifetime and the total carrier recombination lifetime before measurement of the electroluminescence polarization from the quantum well. Spin lifetime, deriving from spin relaxation, will clearly affect the measured polarization. However, the recombination lifetime also plays a critical role, especially in the case of optical detection from semiconductors. Mainly, a longer carrier lifetime translates into a longer time for spin relaxation to occur, leading to lower measured values of electroluminescence polarization. Returning to eqn. 5.1, if  $\tau_r \gg \tau_s$ , most of the injected electrons will relax in spin before recombining with holes, and  $P_{measured} \rightarrow 0$ .

### 5.1.1 Temperature dependence of spin lifetime

The D'yakonov-Perel' (DP) mechanism has been shown to be the most important spin relaxation mechanism in low doped GaAs systems [60]. Within a quantum well,

the first order term for the DP spin relaxation rate is proportional to the momentum scattering time and temperature [98, 108, 112, 113]. Deriving from its inverse dependence on the momentum scattering rate, the DP spin relaxation rate will have a qualitative trend similar to carrier mobility, which generally goes through a peak with temperature [114]. Thus, theoretical predictions based on the DP mechanism in a GaAs(100) quantum well show that the spin relaxation rate for spins aligned perpendicular to the film plane will go through a peak with temperature [98]. This peak in the relaxation rate would correspond to a dip in the measured electroluminescence polarization. However, theoretical work on the spin lifetime dependencies on mobility, quantization energy, and temperature has shown that the peak in the relaxation rate will not result in a significant rise in the spin lifetime at higher temperatures [115]. Indeed, attempts to model the DP mechanism based on momentum scattering, using eqn. 5.1 and assuming a constant recombination lifetime, are unable to reproduce the sharp rise seen in the temperature dependence of the electroluminescence polarization at elevated temperatures [116].

Note, the second order term for the DP spin relaxation rate decreases with increasing temperature, opposing the first order term [112, 113]. The DP spin relaxation rate in a GaAs(100) quantum well can be expressed as [113]:<sup>1</sup>

$$\begin{aligned} \frac{1}{\tau_z} = \frac{4\tau_p}{\hbar^2} & \left[ (\alpha_R^2 + \gamma_D^2 \langle k_z^2 \rangle^2) \left( \frac{2m_e k_B T}{\hbar^2} \right) \right. \\ & - (\delta + 2) \gamma_D^2 \langle k_z^2 \rangle \left( \frac{2m_e k_B T}{\hbar^2} \right)^2 \\ & \left. + (\delta + 2)(\delta + 3) \frac{1 + \nu_1/\nu_3}{16} \gamma_D^2 \left( \frac{2m_e k_B T}{\hbar^2} \right)^3 \right] \end{aligned} \quad (5.3)$$

where  $z$  is defined as the growth and confinement direction for the quantum well and  $\tau_z^{-1}$  is the spin relaxation rate for spins aligned perpendicular to the film plane. The

---

<sup>1</sup>See section 1.2.3 and Appendix A for details on eqn. 5.3.

first and second order terms would give rise to a peak in the spin relaxation rate. The third order term is consistent with the temperature dependence of the spin relaxation rate in bulk material [60]. However, meaningful quantitative analysis using eqn. 5.3 is limited by the numerous unknown material constants including the Dresselhaus coupling factor ( $\gamma_D$ ) for quantum wells.<sup>2</sup> In addition, the momentum scattering time ( $\tau_p$ ) has a temperature dependence that is difficult to model in a quantum well system and is normally obtained empirically by measuring the carrier mobility.

### 5.1.2 Temperature dependence of recombination lifetime

The total carrier recombination lifetime within the quantum well, given by eqn. 5.2, while difficult to model quantitatively, is expected to have a temperature dependence that goes through a peak with temperature. At low temperatures, the total recombination lifetime will first increase with increasing temperature as the radiative lifetime becomes longer. Qualitatively, this effect arises because increasing thermal energy works against the formation of electron-hole pairs. Continuing to increase the temperature will eventually lead to a peak in the total recombination lifetime as nonradiative pathways become activated, leading to a decrease in the overall carrier lifetime. These temperature trends for the radiative, nonradiative, and overall recombination lifetimes have been observed experimentally in GaAs quantum wells [118, 119]. Note that a peak in the total recombination lifetime would lead to a nonmonotonic temperature dependence in the electroluminescence polarization, as longer total carrier lifetimes translate into more time for electrons to relax in spin before they are measured optically from the quantum well or are removed from the system by a nonradiative pathway.

Observing the temperature dependence of the electroluminescence intensity, as shown in fig 5.1 for an 8% Al *p-i-p* sample, the recombination lifetime likely plays a

---

<sup>2</sup>Bulk values, however, have been estimated, for example see Ref. [117].

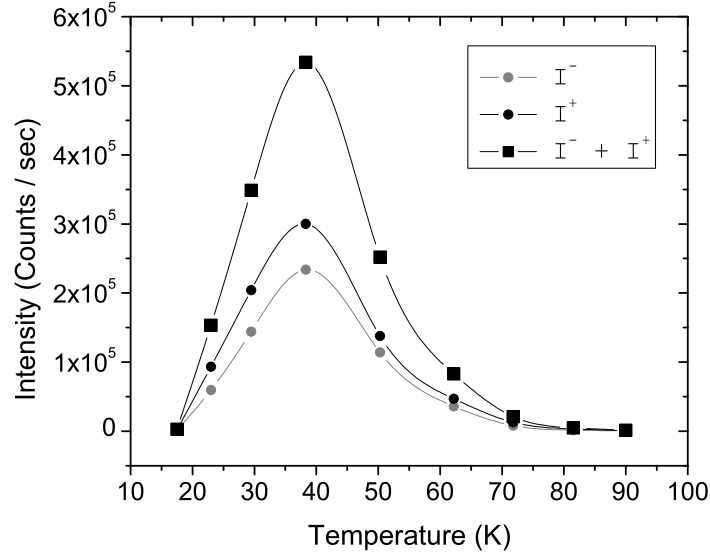


Figure 5.1: Integrated electroluminescence intensity vs. temperature for an 8% Al *p-i-p* sample, for  $I^+$  (left-hand) and  $I^-$  (right-hand) circularly polarized light.

significant role in the final measured polarization. Although, since the electroluminescence measures only radiative emission recombination, the intensities shown in fig. 5.1 are actually a measure of the total recombination lifetime divided by the radiative component ( $\tau_r/\tau_{rad}$ ).

## 5.2 Time Resolved Optical Studies

Time resolved optical techniques can be used to obtain quantitative experimental data on both the spin lifetime and total recombination lifetime in the GaAs sample structures. Time resolved Kerr rotation measures the effective spin lifetime of the carriers in a sample, where the effective spin lifetime ( $\tau_s^*$ ) is defined as:

$$\tau_s^{*-1} = \tau_s^{-1} + \tau_r^{-1}. \quad (5.4)$$

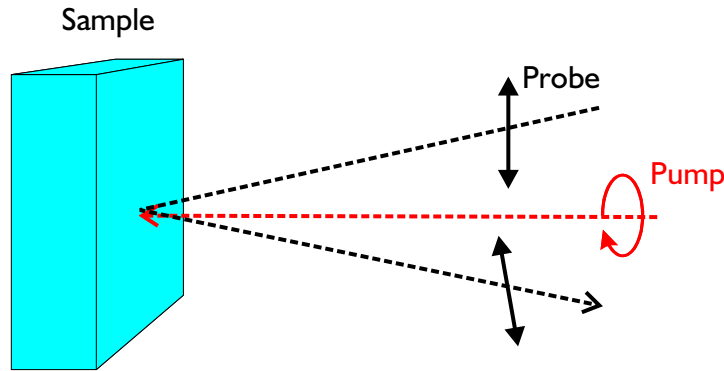


Figure 5.2: Illustration of the time resolved Kerr rotation measurement.

An illustration of the measurement is shown in fig. 5.2. A circularly polarized pump beam, propagating perpendicular to the film plane, creates a population of spin polarized carriers with spins aligned perpendicular to the film plane within the quantum well. The pump beam is followed by a linearly polarized probe beam, which is reflected off the sample. Owing to the magneto-optical Kerr effect, the major polarization axis of the probe beam is rotated by an angle proportional to the electron spin polarization in the quantum well. By varying the delay between the pump and probe beam, this technique measures the effective spin lifetime  $\tau_s^*$  inside the quantum well.

In a similar setup to time resolved Kerr rotation, time resolved differential reflectivity can be used to measure the total carrier lifetime. After the pump beam creates a population of carriers within the sample, the reflected intensity of the probe beam, which is dependent on the carrier population, is then measured. By varying the delay between the pump and probe beam, this technique measures the total carrier recombination lifetime  $\tau_r$ . Together with the effective spin lifetime measurement obtained from Kerr rotation, the spin lifetime  $\tau_s$  can then be extracted using eqn. 5.4.

### 5.3 Experimental Setup

Both time resolved Kerr rotation and differential reflectivity experiments were conducted on the same AlGaAs-GaAs quantum well samples that produced the measured electroluminescence polarizations reported in chapter 4. The samples were placed in an optical cold-finger cryostat and a single bias voltage ( $V_T$ ), applied across the entire structure, was used in an experimental setup consistent with the sample setup described in section 4.2. A circularly polarized pump beam and a linearly polarized probe beam from a mode-locked Ti:sapphire laser were focused to overlapping spots on the CoFe-MgO spin injector with an angle of incidence of  $\sim 5^\circ$ . The diameter of the probe beam was  $\sim 20 \mu\text{m}$  with a power of  $8 \mu\text{W}$ , while the pump beam had a slightly broader diameter and a power of  $80 \mu\text{W}$ . The circularly polarized pump beam was tuned to the heavy-hole absorption peak, and thus was capable of creating a highly spin polarized population of electrons in the quantum well [60]. The delay between the pump beam and the 2 ps long probe beam pulses was varied between 150 and 3000 ps using a retroreflecting mirror on a translation stage. Using lock-in techniques, only the pump-induced Kerr rotation of the linearly polarized probe beam was measured in a balanced bridge setup, thus eliminating the background Kerr rotation from the ferromagnetic electrode. Pump-induced changes in the reflected probe beam intensity were monitored simultaneously by additional lock-in amplifiers. Finally a magnetic field was applied perpendicular to the film plane, but was limited to magnitudes of less than 0.8 T in the setup.

### 5.4 Experimental Results and Discussion

Figure 5.3 shows example fits of the time resolved Kerr rotation (KR) and differential reflectivity (DR) for a 16% Al *p-i-p* AlGaAs-GaAs quantum well sample at 25 K and

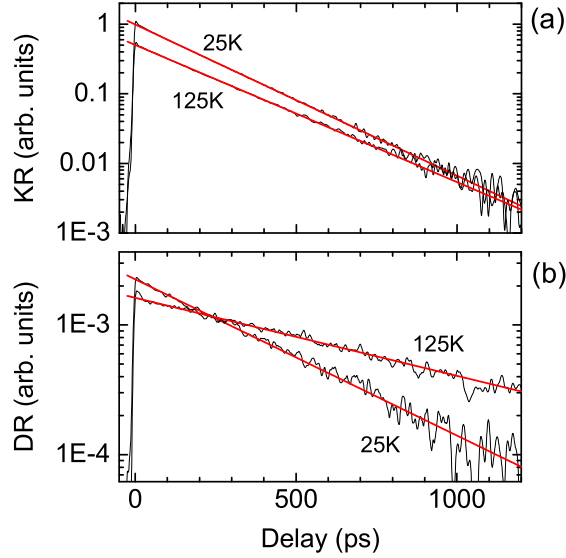


Figure 5.3: Time resolved Kerr rotation (a) and differential reflectivity (b) for a 16% Al  $p$ - $i$ - $p$  sample measured at 25 and 125 K with  $V_T = 2.0$  V and 0.8 T applied magnetic field. The exponential decay of the KR signal is determined by both spin decay and carrier recombination, while the DR signal decays solely due to carrier recombination. Solid straight lines represent exponential fits to the KR and DR signals.

125 K, with  $V_T = 2.0$  V and 0.8 T applied perpendicular magnetic field. Both the KR and the DR decay exponentially, where the exponential fit to the KR data extracts the effective spin lifetime  $\tau_s^*$  and the fit to the DR result gives the total recombination lifetime  $\tau_r$ . The fits in fig. 5.3 give  $\tau_s^* = 200(220)$  ps and  $\tau_r = 360(722)$  ps at 25(125) K.

The measured effective spin lifetime  $\tau_s^*$  and recombination lifetime  $\tau_r$  are shown together with spin lifetime  $\tau_s$  in fig. 5.4(a) for a 16% Al  $p$ - $i$ - $p$  sample. Solid symbols refer to data at 0 T while open symbols refer to measurements with an applied magnetic field of 0.8 T. The spin lifetime, in general, decreases with increasing temperature, although a small inflection point occurs between 100-150 K. These results are consistent with the theoretical work presented in Ref. [115]. The recombination

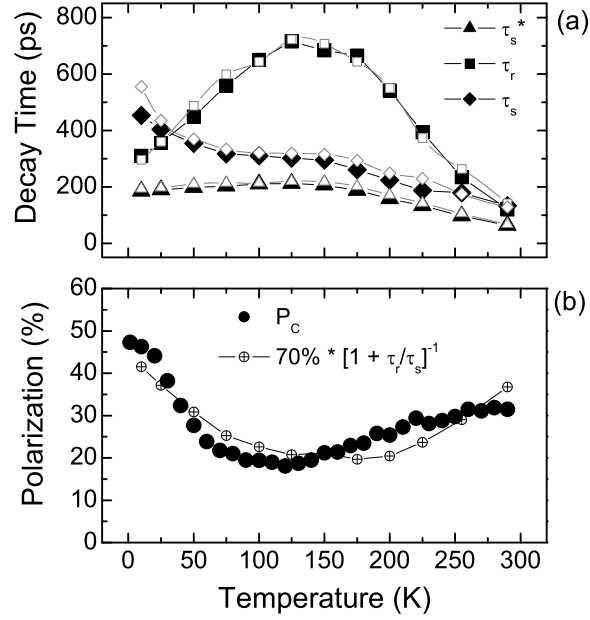


Figure 5.4: (a) Measured  $\tau_s^*$ ,  $\tau_r$ , and  $\tau_s$  vs. temperature for a 16% Al *p-i-p* sample with  $V_T = 2.0$  V. Solid and open symbols are for 0 T and 0.8 T magnetic fields, respectively. (b) Background corrected electroluminescence polarization  $P_C$  from electrical spin injection and the expected measured polarization for  $\sim 70\%$  injected spin polarization using the spin and recombination lifetimes measured at 0 T.

lifetime, however, displays a peak with temperature. This peak, deriving from radiative and nonradiative lifetime temperature characteristics described in section 5.1.2, is likely the source of the nonmonotonic temperature dependence seen in the electroluminescence polarization. A small magnetic field dependence appears in the measured lifetimes. However, a thorough analysis is limited by the maximum magnetic field of 0.8 T in this experimental setup.

In fig. 5.4(b), the background corrected polarization  $P_C$ , obtained from electrical injection, is plotted on the same scale as a curve for an assumed 70% injected polarization extracted from the lifetimes in fig. 5.4(a) at 0 T and eqn. 5.1. The similarity of the two curves indicates that electrical spin injection from the CoFe-MgO is  $\sim 70\%$  over a large temperature range up to room temperature. The injected polarization

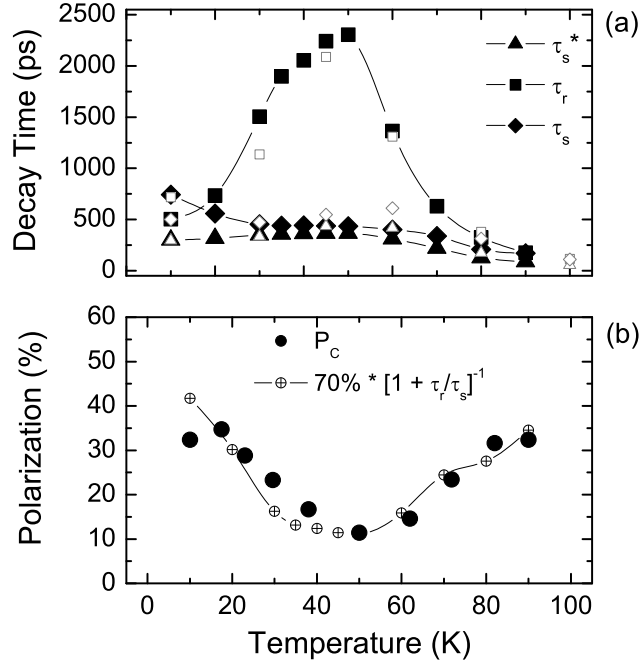


Figure 5.5: (a) Measured  $\tau_s^*$ ,  $\tau_r$ , and  $\tau_s$  vs. temperature for an 8% Al *p-i-p* sample with  $V_T = 1.9$  V. Solid and open symbols are for 0 T and 0.8 T magnetic fields, respectively. (b) Corrected electroluminescence polarization  $P_C$  from electrical spin injection and the expected measured polarization for  $\sim 70\%$  injected spin polarization using the spin and recombination lifetimes measured at 0 T.

has a much smaller temperature dependence than the nonmonotonic temperature dependence seen in the electroluminescence polarization, which derives from a peak in the recombination lifetime inside the semiconductor quantum well. Similar results are shown for an 8% Al *p-i-p* sample in fig. 5.5, where the peak in the recombination lifetime results in a nonmonotonic temperature dependence in the measured polarization, while the injected polarization is relatively temperature independent at  $\sim 70\%$ . Note, for the measurements in fig. 5.4 and fig. 5.5, the applied bias voltage  $V_T$  is set to mimic the bias voltage conditions of the electrical injection experiments.

While the optical studies provide useful insight into the effects of the spin and recombination lifetimes on the electroluminescence polarization, the experiment still

differs from electrical injection. In electrical injection, spin polarized electrons are injected ballistically into GaAs and recombine with holes from the substrate. The optical experiments create electrons and holes simultaneously in the quantum well, likely leading to a different band profile than for electrical injection. Also,  $P_C$  is the measured electroluminescence polarization after subtraction of a magnetic field dependent background signal, and represents an effective zero field result for data obtained at a finite field. The lifetimes used to calculate the expected polarization in fig. 5.4(b) and fig. 5.5(b) are actual zero field lifetimes. Overall, the variation in experimental setup and conditions between electrical injection and the optical studies likely contribute to the quantitative differences seen in the two experiments.

## 5.5 Summary

In this study, time resolved Kerr rotation, differential reflectivity, and electrical spin injection experiments on GaAs quantum well spin detectors directly measure the effects of spin and carrier recombination lifetime on the electroluminescence polarization in spin injection experiments. Understanding lifetime effects within the semiconductor is essential for the development of semiconductor spintronic devices. While both spin and carrier recombination lifetimes affect the measured polarization from spin injection, a peak in the temperature dependence of the total recombination lifetime is found to correspond to the dip observed in the temperature dependence of the electroluminescence polarization. These results show that the electrical spin injection efficiency from CoFe-MgO spin injectors exhibits a much smaller temperature dependence than the dramatic nonmonotonic behavior of the electroluminescence polarization. In addition, the time resolved studies indicate that the CoFe-MgO spin injectors retain a high spin injection efficiency of  $\sim 70\%$  for a wide temperature range from 10 K up to room temperature.



# Chapter 6

## Conclusion

Pioneering results on electron and hole spin diffusion lengths and spin lifetimes within GaAs in the late 1990's sparked the growth of a novel field of research called spintronics. This development, in combination with the daunting power density issues facing conventional semiconductor technologies, resulted in a broad scientific effort to explore electron spin related phenomena with the hope of eventually producing useful spin-based technologies.

By utilizing the spin property of electrons, spintronic devices have the potential for much smaller sizes and lower power densities than their charge-based counterparts. Semiconductors remain attractive because of the extensive knowledge in semiconductor physics already obtained with conventional technologies, the lack of a large background population of unpolarized electrons, the extensive manufacturing base, and the prospect of integrating spin devices with conventional devices for optimal functionality. Scientifically, spin transport and dynamics within semiconductors offers an enriching field of research, combining aspects of magnetism, optics, and electronics.

Experimentally, the initial step to developing a spintronic device is electrical spin injection. In order to study and potentially utilize spins in a semiconducting material, a method is needed to create a population of spin polarized carriers inside

the semiconductor. Ideally, the source of spin injection would have to demonstrate efficient spin injection at room temperature. Other desirable characteristics include robustness in fluctuating environment operating conditions, easy fabrication for a potential need of high throughput, and also a dual functionality as a possible detector or filter for spin polarized current. The spin detector concept begins to bridge the gap between electrical spin injection and electrical spin detection, which is viewed as a second important step to developing a spintronic device. Indeed, the optical detection techniques generally used for detecting spins in spin injection experiments are not practical for device application and require large magnetic fields.

The magnetic tunnel transistor spin injector has demonstrated a lower bound injected spin polarization of  $\sim 10\%$  at 1.4 K measured from electroluminescence polarization in a magnetic field after subtraction of a linear background signal. One of the advantages of the MTT is that it has three terminals that can vary both the emitter-to-base and the collector-to-base bias voltage. The emitter-to-base voltage can vary the energy of the ballistically injected electrons while the collector-to-base voltage controls the band bending within the semiconductor collector. The drawback of the MTT is the low injected current into the semiconductor after electrons tunnel from emitter to base, traverse the spin filtering base layer, and then overcome the Schottky barrier at the base-collector interface. The low injected current magnitude enables measurements only at low temperatures and high ( $\sim 2$  V) emitter-to-base bias voltage to attain a sufficient signal-to-noise ratio in the electroluminescence signal. These limitations prevented an extended study of the MTT spin injector, for example, at lower emitter-to-base voltages where a much higher spin polarization of the injected current is expected based on magnetocurrent measurements.

Note that the MTT remains a useful device for the study of spins in semiconductors, although it is limited in the present spin injection studies by the optical detection scheme. The low injected electron current magnitudes may not present a problem in

an eventual application or device, depending on the mode of spin detection. The three terminals offer tuning of the electron energies in the electrical transport, which can be used to affect both the injected spin polarizations as well as the spin dynamics and relaxation rates within the semiconductor. For example, an interesting experiment would be to use the base layer as a Schottky tunneling spin injector and then vary the emitter-to-base bias to alter the spin polarization profile of the injected electrons.

The CoFe-MgO tunnel spin injector has achieved most of the primary goals of spin injection by demonstrating, from electroluminescence, a lower bound injected polarization exceeding 30% at 290 K, while showing good thermal stability withstanding exposures up to 400 °C. Figure 6.1 shows the reported injected polarizations from various spin injector sources to provide a perspective for the results achieved in this work with the CoFe-MgO injector. Note, the points in fig. 6.1 include only results using direct optical detection of injected spins from electroluminescence polarization, and omits measurements that extract the injected polarization indirectly.<sup>1</sup>

The CoFe-MgO spin injectors, as well as the MTT spin injectors, are grown via magnetron sputtering, a deposition technique capable of producing a high throughput of spin injectors if needed. An additional advantage of the CoFe-MgO injector is that the tunneling barrier thickness can be varied for a desired resistance, making the injector potentially more versatile and scalable. Thorough analysis of the spin injection from CoFe-MgO reveals important effects of both spin and carrier recombination lifetime on the optically measured polarization. Specifically, the electroluminescence polarization shows a dramatic nonmonotonic temperature dependence, displaying a minimum over the measurable temperature range of the quantum well detector. Time resolved optical studies show that the dip in the electroluminescence polarization with

---

<sup>1</sup>An example of an indirect measurement is the  $\sim 70\%$  value reported in chapter 5, which is obtained from fitting spin and carrier lifetime effects to the direct electroluminescence measurement.

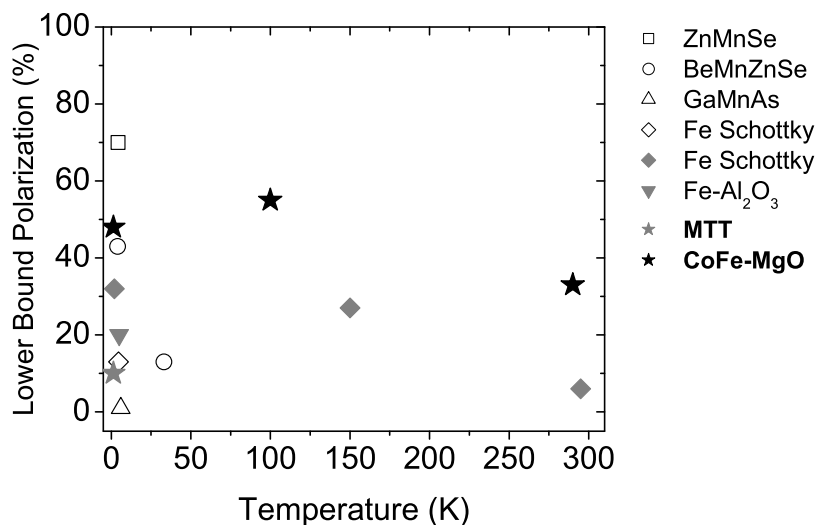


Figure 6.1: Achieved, optically measured, lower bound injected spin polarizations from ZnMnSe [74], BeMnZnSe [77], GaMnAs [78], Fe Schottky [85,89], Fe-Al<sub>2</sub>O<sub>3</sub> [120], MTT, and CoFe-MgO spin injectors. Open symbols represent results achieved by the end of 2001, while the closed symbols are results achieved by 2005.

temperature derives from a peak in the carrier recombination lifetime with temperature in the quantum well detector. More importantly, measurements of the spin and carrier recombination lifetime suggest that the spin injection from the CoFe-MgO injector is  $\sim 70\%$  from 10 K up to room temperature, showing a much smaller dependence on temperature than the electroluminescence polarization.

As stated previously, the large magnetic fields, on the order of a few tesla, in the spin injection experiments are not fundamental to the spin injection structure, but are a requirement of the optical spin detector and the detection scheme under Faraday geometry. For potential applications not requiring optical measurement with Faraday geometry, the spin injectors are likely to have their net magnetic moment aligned in the film plane along their easy axis, requiring magnetic fields on the order of millitesla, rather than tesla. In this scenario, injected spins would be aligned parallel to the film plane and spin polarized current can be injected even under remnant magnetization

of the spin injectors in the absence of a magnetic field.

With the development of a robust, room temperature spin injector, future work aims to develop an electrical spin detector. The CoFe-MgO is being studied as a possible detector for spin polarized current and devices having CoFe-MgO structures as both a spin injector and a spin detector are being investigated. Additional experimental effort is also being devoted to measuring the spin dynamics of electron spins moving inside semiconductor channels using time resolved optical techniques such as Kerr rotation. An example test structure would be a semiconductor channel region (either silicon-on-insulator, two-dimensional electron gas, or a membrane of GaAs or Si) with both a spin injector and a spin detector separated by a finite distance. Electron spins would then be injected into the channel and then extracted at the detector, where a magnetoresistive effect should arise depending on the magnetizations of the injector and detector. Magneto-optical Kerr rotation can be used to characterize spin transport within the channel region while optical pumping and spin extraction magneto-effects can characterize spin tunneling from the semiconductor into metals.

For the field of spintronics as a whole, a means of electrical detection is the next critical challenge. While ideas for detection of spin polarized current are available, a method of reading and interpreting spins for information processing remains undiscovered. However, concerning spin injection, the CoFe-MgO spin injectors developed in this dissertation have completed the first stage in research towards a spintronics device technology by providing highly efficient, robust, room temperature spin injectors that can be fabricated with high throughput. Both the MTT and CoFe-MgO spin injectors have the potential to play a crucial role in the experimental study of spin properties within semiconductors, and possibly represent precursors to actual components in eventual spintronic devices.



# Appendix A

## D'yakonov-Perel' spin relaxation in GaAs(100) quantum wells

This appendix is adapted from a full derivation of the D'yakonov-Perel' (DP) spin relaxation rate in GaAs(100) quantum wells<sup>1</sup> by Anthony Ndirango [113] and is included here with the permission of Mr. Ndirango. Ndirango notes that the material presented below, although not published in this form, was well understood by the original authors who developed the equations for DP spin relaxation in Refs. [60,108,121].

### A.1 Derivation of Equation 5.3

The macroscopic spin polarization of an ensemble can be modeled as [113]

$$S_\alpha(t) = \sum_{\mathbf{k}} Tr\{\rho(E_{\mathbf{k}}; t)\sigma_\alpha\}, \quad \alpha = x, y, z \quad (\text{A.1})$$

---

<sup>1</sup>This derivation assumes elastic, spin independent, and spin conserving scattering for nondegenerate electrons.

where  $\{\sigma_x, \sigma_y, \sigma_z\}$  are the Pauli matrices,  $\rho(E_{\mathbf{k}}; t)$  is a density matrix that characterizes the spin state of the system, and the trace ( $Tr$ ) is a  $(2 \times 2)$  matrix trace over *spin-space*. The evolution of the density matrix is given by [60, 113, 122]

$$\frac{\partial \rho(E_{\mathbf{k}}; t)}{\partial t} = -\frac{1}{\hbar^2} \sum_{n=-\infty}^{\infty} \frac{1}{\nu_n(E_{\mathbf{k}})} [\hat{H}_{-n}, [\hat{H}_n, \rho(E_{\mathbf{k}}; t)]] \quad (\text{A.2})$$

where

$$\begin{aligned} \hat{H}_n &\equiv \int_0^{2\pi} \frac{1}{2\pi} \hat{H}_{so}(\mathbf{k}) \exp(-in\varphi_{\mathbf{k}}) d\varphi_{\mathbf{k}} , & \tan(\varphi_{\mathbf{k}}) &\equiv \frac{k_y}{k_x} \\ \nu_n(E_{\mathbf{k}}) &\equiv \int_0^{2\pi} \Gamma_{\mathbf{k} \rightarrow \mathbf{k}'} (1 - \cos(n\theta_{\mathbf{k}\mathbf{k}'})) d\theta_{\mathbf{k}\mathbf{k}'} , & \theta_{\mathbf{k}\mathbf{k}'} &\equiv \varphi_{\mathbf{k}} - \varphi_{\mathbf{k}'} \end{aligned}$$

and  $\Gamma_{\mathbf{k} \rightarrow \mathbf{k}'}$  is the momentum scattering rate.  $\Gamma_{\mathbf{k} \rightarrow \mathbf{k}'}$  can be modeled with a power law,  $\Gamma_{\mathbf{k} \rightarrow \mathbf{k}'} \sim |\mathbf{k} - \mathbf{k}'|^{-2\delta}$ , where  $\delta$  is a constant determined by the source(s) of scattering. Assuming a parabolic dispersion relation ( $\hbar^2 k^2 = 2m^* E_{\mathbf{k}}$ ,  $m^*$  is effective mass) while considering only elastic scattering yields the following:

$$\begin{aligned} |\mathbf{k} - \mathbf{k}'|^2 &= k^2 - 2kk' \cos(\theta_{\mathbf{k}\mathbf{k}'}) + k'^2 = \frac{2m^*}{\hbar^2} E_{\mathbf{k}} (1 - \cos(\theta_{\mathbf{k}\mathbf{k}'})) \\ \implies \Gamma_{\mathbf{k} \rightarrow \mathbf{k}'} &\sim |\mathbf{k} - \mathbf{k}'|^{-2\delta} = \frac{\hbar^{2\delta}}{(2m^*)^\delta} E_{\mathbf{k}}^{-\delta} \frac{1}{(1 - \cos(\theta_{\mathbf{k}\mathbf{k}'}))^\delta} \end{aligned} \quad (\text{A.3})$$

Using this expression for  $\Gamma_{\mathbf{k} \rightarrow \mathbf{k}'}$  to find  $\nu_n(E_{\mathbf{k}})$  in the third line of eqn. A.2 results in

$$\nu_n(E_{\mathbf{k}}) = \zeta_n E_{\mathbf{k}}^{-\delta} \quad (\text{A.4})$$

where  $\zeta_n$  is a real, constant coefficient.

Returning to equation A.2 and combining it with eqn. A.1 produces

$$\begin{aligned} \frac{\partial S_\alpha(t)}{\partial t} &= \sum_{\mathbf{k}} Tr \left\{ \frac{\partial \rho(E_{\mathbf{k}}; t)}{\partial t} \sigma_\alpha \right\} \\ &= -\frac{1}{\hbar^2} \sum_{\mathbf{k}} \sum_{n=-\infty}^{\infty} \frac{1}{\nu_n(E_{\mathbf{k}})} Tr \left\{ [\hat{H}_{-n}, [\hat{H}_n, \rho(E_{\mathbf{k}}; t)]] \sigma_\alpha \right\} \end{aligned} \quad (\text{A.5})$$

which can be converted to the following form [60, 112, 113, 122]

$$\frac{\partial S_\alpha(t)}{\partial t} = - \sum_{\beta} (\tau^{-1})_{\alpha\beta} S_\beta(t), \quad \beta = x, y, z \quad (\text{A.6})$$

with

$$(\tau^{-1})_{\alpha\beta} \equiv \frac{\int \varrho_{DOS}(E) [F_+(E) - F_-(E)] \Omega_{\alpha\beta}(E) dE}{\int \varrho_{DOS}(E) [F_+(E) - F_-(E)] dE}$$

$$\Omega_{\alpha\beta}(E) \equiv \frac{\pi}{\hbar^2} \sum_{n=-\infty}^{\infty} \frac{1}{\nu_n(E)} Tr \left\{ [\hat{H}_{-n}, [\hat{H}_n, \sigma_\beta]] \sigma_\alpha \right\}$$

$$F_\pm(E) \equiv \frac{1}{1 + \exp[\eta(E - \mu_\pm)]}, \quad \eta \equiv \frac{1}{k_B T}$$

where  $\varrho_{DOS}(E)$  represents the density of states at energy  $E$ ,  $k_B$  is Boltzmann's constant, and  $\mu_{+(-)}$  is the chemical potential for "spin up (down)" electrons. Now, if the spin-splitting is small such that  $|\mu_+ - \mu_-| \ll |\mu_\pm|$ , where  $\mu_\pm = \mu_0 \pm \frac{\Delta}{2}$  and  $\mu_0$  is the equilibrium chemical potential, one can approximate

$$F_+(E) - F_-(E) \approx \Delta \frac{\partial F_0}{\partial E}, \quad F_0(e) \equiv \frac{1}{1 + \exp[\eta(E - \mu_0)]}$$

Using this simplification,  $(\tau^{-1})_{\alpha\beta}$  in eqn. A.6 becomes

$$(\tau^{-1})_{\alpha\beta} = \frac{\int \varrho_{DOS}(E) \frac{\partial F_0}{\partial E} \Omega_{\alpha\beta}(E) dE}{\int \varrho_{DOS}(E) \frac{\partial F_0}{\partial E} dE} \quad (\text{A.7})$$

The expression for the spin-orbit Hamiltonian ( $\hat{H}_{so} = \hat{H}_{Dresselhaus} + \hat{H}_{Rashba}$ ) using equations 1.21 and 1.22 yields the following characteristics for  $\Omega_{\alpha\beta}$

$$\begin{aligned} \Omega_{xx}(E) &= \Omega_{yy}(E) \\ \Omega_{xy}(E) &= -\Omega_{yx}(E) \\ \Omega_{xz}(E) &= \Omega_{zx}(E) = \Omega_{zy}(E) = \Omega_{yz}(E) = 0 \end{aligned}$$

As a result, the only non-zero components of  $(\tau^{-1})$  are

$$\begin{aligned} (\tau^{-1})_{xx} &= (\tau^{-1})_{yy} \\ (\tau^{-1})_{xy} &= -(\tau^{-1})_{yx} \\ (\tau^{-1})_{zz} & \end{aligned}$$

With this knowledge, eqn. A.6 can now be written as

$$\frac{\partial S_z(t)}{\partial t} = -(\tau^{-1})_{zz} S_z(t) \quad (\text{A.8})$$

$$\frac{\partial S_{\pm}(t)}{\partial t} = -(\tau^{-1})_{\pm} S_{\pm}(t) \quad (\text{A.9})$$

where  $S_{\pm} \equiv S_x \pm S_y$  and  $(\tau^{-1})_{\pm} \equiv (\tau^{-1})_{xx} \pm (\tau^{-1})_{yx}$ . Under this scenario,  $\tau_z$  represents the spin relaxation time for spins aligned with the [100]-directional axis, while  $\tau_+$  and  $\tau_-$  are the spin relaxation times for spins aligned with the [110] and  $[1\bar{1}0]$ -directional axes, respectively. Finally, with all the pieces in eqn. A.6 defined, one can derive the

following expressions for  $\tau_z$  and  $\tau_{\pm}$ :

$$\frac{1}{\tau_z} = \frac{4\tau_p}{\hbar^2} \left[ (\alpha_R^2 + \gamma_D^2 \langle k_z^2 \rangle) \left( \frac{2m^* k_B T}{\hbar^2} \right) - (\delta + 2) \gamma_D^2 \langle k_z^2 \rangle \left( \frac{2m^* k_B T}{\hbar^2} \right)^2 + (\delta + 2)(\delta + 3) \frac{1 + \nu_1/\nu_3}{16} \gamma_D^2 \left( \frac{2m^* k_B T}{\hbar^2} \right)^3 \right]$$

$$\frac{1}{\tau_{\pm}} = \frac{2\tau_p}{\hbar^2} \left[ (\alpha_R^2 \mp \gamma_D^2 \langle k_z^2 \rangle) \left( \frac{2m^* k_B T}{\hbar^2} \right) \pm (\delta + 2) \gamma_D (\alpha_R \mp \gamma_D \langle k_z^2 \rangle) \left( \frac{2m^* k_B T}{\hbar^2} \right)^2 + (\delta + 2)(\delta + 3) \frac{1 + \nu_1/\nu_3}{16} \gamma_D^2 \left( \frac{2m^* k_B T}{\hbar^2} \right)^3 \right]$$

where T is temperature, and

$$\tau_p \equiv \frac{\int \varrho_{DOS}(E) \frac{\partial F_0}{\partial E} \frac{1}{\nu_1(E)} dE}{\int \varrho_{DOS}(E) \frac{\partial F_0}{\partial E} dE}$$

represents the momentum relaxation time. The calculation assumes  $\tau_p \ll \tau_z, \tau_{\pm}$ . This parameter is generally expressed with its relation to electron mobility,  $\mu_p = q\tau_p/m^*$ , which can be measured empirically. Note,  $\nu_n$  is the momentum scattering rate defined in eqn. A.2. Also, from the expressions in equations A.2 and A.3

$$\frac{\nu_1}{\nu_3} = \begin{cases} \frac{(2-\delta)(3-\delta)}{\delta^2-\delta+6}, & \delta < \frac{3}{2} \\ \frac{1}{9}, & \delta \geq \frac{3}{2} \end{cases}.$$



# Bibliography

- [1] P. M. Tedrow and R. Meservey, Phys. Rev. B **7**, 318 (1973).
- [2] P. M. Tedrow and R. Meservey, Phys. Rev. Lett. **27**, 919 (1971).
- [3] M. Julliere, Phys. Lett. **54A**, 225 (1975).
- [4] G. A. Gibson and R. Meservey, J. Appl. Phys. **58**, 1584 (1985).
- [5] T. Miyazaki and N. Tezuka, J. Magn. Magn. Mat. **139**, L231 (1995).
- [6] J. S. Moodera, J. Nassar, and G. Mathon, Annu. Rev. Mater. Sci. **29**, 381 (1990).
- [7] J. S. Moodera, L. R. Kinder, T. M. Wong, and R. Meservey, Phys. Rev. Lett. **74**, 3273 (1995).
- [8] M. K. Ho et al., IEEE Trans. Magn. **37**, 1691 (2001).
- [9] S. S. P. Parkin, in *Annual Review of Materials Science*, edited by B. W. Wessels, volume 25, pages 357–388, Annual Reviews Inc., Palo Alto, CA, 1995.
- [10] R. E. Matick, *Computer Storage Systems and Technology*, Wiley, New York, 1977.
- [11] A. H. Eschenfelder, *Magnetic Bubble Technology*, volume 14, Springer, Berlin, 1980.

- [12] J. M. Daughton, *Thin Solid Films* **216**, 162 (1992).
- [13] D. D. Tang, P. K. Wang, V. S. Speriosu, S. Le, and K. K. Kung, *IEEE Trans. Magn.* **31**, 3206 (1995).
- [14] S. S. P. Parkin et al., *J. Appl. Phys.* **85**, 5828 (1999).
- [15] S. S. P. Parkin et al., *Proc. IEEE* **91**, 661 (2003).
- [16] N. F. Mott, *Proc. R. Soc. London, Ser. A* **153**, 699 (1936).
- [17] N. F. Mott, *Proc. R. Soc. London, Ser. A* **156**, 368 (1936).
- [18] A. Fert and I. A. Campbell, *Phys. Rev. Lett.* **21**, 1190 (1968).
- [19] I. A. Campbell, A. Fert, and A. R. Pomeroy, *Philos. Mag.* **15**, 977 (1967).
- [20] S. Zhang, P. M. Levy, A. C. Marley, and S. S. P. Parkin, *Phys. Rev. Lett.* **79**, 3744 (1997).
- [21] J. C. Slonczewski, *Phys. Rev. B* **39**, 6995 (1989).
- [22] J. C. Slonczewski, *Phys. Rev. B* **71**, 024411 (2005).
- [23] J. Mathon and A. Umerski, *Phys. Rev. B* **63**, 220403(R) (2001).
- [24] W. H. Butler, X.-G. Zhang, T. C. Schulthess, and J. M. MacLaren, *Phys. Rev. B* **63**, 054416 (2001).
- [25] X.-G. Zhang and W. H. Butler, *Phys. Rev. B* **70**, 172407 (2004).
- [26] R. Meservey and P. M. Tedrow, *Phys. Rep.* **238**, 173 (1994).
- [27] W. H. Butler, X.-G. Zhang, T. C. Schulthess, and J. M. MacLaren, *Phys. Rev. B* **63**, 092402 (2001).

- [28] I. Žutić, J. Fabian, and S. D. Sarma, *Rev. Mod. Phys.* **76**, 323 (2004).
- [29] R. C. O’Handley, *Modern Magnetic Materials: Principles and Applications*, John Wiley & Sons, Inc., New York, 2000.
- [30] M. Sharma, S. X. Wang, and J. H. Nickel, *Phys. Rev. Lett.* **82**, 616 (1999).
- [31] J. M. D. Teresa et al., *Phys. Rev. Lett.* **82**, 4288 (1999).
- [32] A. Yelon, *Physics of Thin Films: Advances in Research and Development*, volume 6, Academic, New York, 1971.
- [33] D. P. Pappas et al., *Phys. Rev. Lett.* **66**, 504 (1991).
- [34] G. Schönhense and H. C. Siegmann, *Ann. Phys.-Leipzig* **2**, 465 (1993).
- [35] M. Getzlaff, J. Bansmann, and G. Schönhense, *Solid State Commun.* **87**, 467 (1993).
- [36] J. C. Gröbli, D. Guarisco, S. Frank, and F. Meier, *Phys. Rev. B* **51**, 2945 (1995).
- [37] E. Vescovo et al., *Phys. Rev. B* **52**, 13497 (1995).
- [38] H. J. Drouhin, A. J. vander Sluijs, Y. Lassaily, and G. Lampel, *J. Appl. Phys.* **79**, 4734 (1996).
- [39] A. Filipe et al., *Phys. Rev. Lett.* **80**, 2425 (1998).
- [40] D. Oberli, R. Burgermeister, S. Riesen, W. Weber, and H. C. Siegmann, *Phys. Rev. Lett.* **81**, 4228 (1998).
- [41] M. Aeschlimann et al., *Phys. Rev. Lett.* **79**, 5158 (1997).

- [42] R. Knorren, K. H. Bennemann, R. Burgermeister, and M. Aeschlimann, *Phys. Rev. B* **61**, 9427 (2000).
- [43] W. H. Rippard and R. A. Buhrman, *Phys. Rev. Lett.* **84**, 971 (2000).
- [44] W. Weber, S. Riesen, and H. C. Siegmann, *Science* **291**, 1015 (2001).
- [45] D. J. Monsma, J. C. Lodder, T. J. A. Popoma, and B. Dieny, *Phys. Rev. Lett.* **74**, 5260 (1995).
- [46] D. J. Monsma, R. Vlutters, and J. C. Lodder, *Science* **281**, 407 (1998).
- [47] P. S. A. Kumar et al., *Physica C* **350**, 166 (2001).
- [48] K. Mizushima, T. Kinno, T. Yamauchi, and K. Tanaka, *IEEE Trans. Magn.* **33**, 3500 (1997).
- [49] R. Sato and K. Mizushima, *Appl. Phys. Lett.* **79**, 1157 (2001).
- [50] E. Zarate, P. Apell, and P. Echenique, *Phys. Rev. B* **60**, 2326 (1999).
- [51] H.-J. Drouhin, *Phys. Rev. B* **62**, 556 (2000).
- [52] H.-J. Drouhin, *J. Appl. Phys.* **89**, 6805 (2001).
- [53] S. van Dijken, X. Jiang, and S. S. P. Parkin, *Appl. Phys. Lett.* **80**, 3364 (2002).
- [54] S. van Dijken, X. Jiang, and S. S. P. Parkin, *Appl. Phys. Lett.* **83**, 951 (2003).
- [55] S. van Dijken, X. Jiang, and S. S. P. Parkin, *Phys. Rev. Lett.* **90**, 197203 (2003).
- [56] X. Jiang, S. van Dijken, R. Wang, and S. S. P. Parkin, *Phys. Rev. B* **69**, 014413 (2004).
- [57] S. van Dijken, X. Jiang, and S. S. P. Parkin, *Phys. Rev. B* **66**, 094417 (2002).

- [58] S. van Dijken, X. Jiang, and S. S. P. Parkin, *Appl. Phys. Lett.* **82**, 775 (2003).
- [59] S. van Dijken, X. Jiang, and S. S. P. Parkin, *J. Appl. Phys.* **97**, 043712 (2005).
- [60] F. Meier and B. P. Zakharchenya, editors, *Optical Orientation*, North-Holland, New York, 1984.
- [61] S. Datta and B. Das, *Appl. Phys. Lett.* **56**, 665 (1990).
- [62] J. M. Kikkawa and D. D. Awschalom, *Phys. Rev. Lett.* **80**, 4313 (1998).
- [63] D. Hägele, M. Oestreich, W. W. Rühle, N. Nestle, and K. Eberl, *Appl. Phys. Lett.* **73**, 1580 (1998).
- [64] J. M. Kikkawa and D. D. Awschalom, *Nature* **397**, 139 (1999).
- [65] D. Loss and D. P. DiVincenzo, *Phys. Rev. A* **57**, 120 (1998).
- [66] I. Žutić, J. Fabian, and S. D. Sarma, *Phys. Rev. Lett.* **88**, 066603 (2002).
- [67] J. Fabian, I. Žutić, and S. D. Sarma, *Phys. Rev. B* **66**, 165301 (2002).
- [68] J. E. Hirsch, *Phys. Rev. Lett.* **83**, 1834 (1999).
- [69] S. Murakami, N. Nagaosa, and S.-C. Zhang, *Science* **301**, 1348 (2003).
- [70] Y. Kato, R. C. Myers, A. C. Gossard, and D. D. Awschalom, *Science* **306**, 1910 (2004).
- [71] J. Wunderlich, B. Kaestner, J. Sinova, and T. Jungwirth, *Phys. Rev. Lett.* **94**, 047204 (2005).
- [72] S. A. Wolf et al., *Science* **294**, 1488 (2001).
- [73] M. Oestreich et al., *Appl. Phys. Lett.* **74**, 1251 (1999).

- [74] R. Fiederling et al., *Nature* **402**, 787 (1999).
- [75] Y. Ohno, R. Terauchi, T. Adachi, F. Matsukura, and H. Ohno, *Phys. Rev. Lett.* **83**, 4196 (1999).
- [76] B. T. Jonker et al., *Phys. Rev. B* **62**, 8280 (2000).
- [77] B. T. Jonker et al., *Appl. Phys. Lett.* **79**, 3098 (2001).
- [78] Y. Ohno et al., *Nature* **402**, 790 (1999).
- [79] G. Schmidt, D. Ferrand, L. W. Molenkamp, A. T. Filip, and B. J. van Wees, *Phys. Rev. B* **62**, 4790 (2000).
- [80] P. R. Hammar, B. R. Bennett, M. J. Yang, and M. Johnson, *Phys. Rev. Lett.* **83**, 203 (1999).
- [81] S. Gardelis, C. G. Smith, C. H. W. Barnes, E. H. Lindfield, and D. A. Ritchie, *Phys. Rev. B* **60**, 7764 (1999).
- [82] C. M. Hu, J. Nitta, A. Jensen, J. B. Hansen, and H. Takayanagi, *Phys. Rev. B* **63**, 125333 (2001).
- [83] H. J. Zhu et al., *Phys. Rev. Lett.* **87**, 016601 (2001).
- [84] P. R. Hammar and M. Johnson, *Appl. Phys. Lett.* **79**, 2591 (2001).
- [85] A. T. Hanbicki, B. T. Jonker, G. Itskos, G. Kioseoglou, and A. Petrou, *Appl. Phys. Lett.* **80**, 1240 (2002).
- [86] T. Manago and H. Akinaga, *Appl. Phys. Lett.* **81**, 694 (2002).
- [87] V. F. Motsnyi et al., *Appl. Phys. Lett.* **81**, 265 (2002).
- [88] A. T. Hanbicki et al., *Appl. Phys. Lett.* **82**, 4092 (2003).

- [89] C. Adelman, X. Lou, J. Strand, C. J. Palmstrm, and P. A. Crowell, *Phys. Rev. B*, 121301(R) (2005).
- [90] E. I. Rashba, *Phys. Rev. B* **62**, 16267(R) (2000).
- [91] D. J. Griffiths, *Introduction to Electrodynamics*, volume 1, Prentice-Hall, Inc., Englewood Cliffs, NJ, 1981.
- [92] G. Dresselhaus, *Phys. Rev.* **100**, 580 (1955).
- [93] E. I. Rashba, *Sov. Phys. Solid State* **2**, 1109 (1960).
- [94] B. Baylac et al., *Solid State Communications* **93**, 57 (1995).
- [95] C. Weisbuch and B. Vinter, *Quantum Semiconductor Structures: Fundamentals and Applications*, Academic, New York, 1991.
- [96] X. Jiang et al., *Phys. Rev. Lett.* **90**, 256603 (2003).
- [97] T. Amand et al., *Phys. Rev. B* **50**, 11624 (1994).
- [98] V. I. Puller, L. G. Mourokh, and N. J. M. Horing, *Phys. Rev. B* **67**, 155309 (2003).
- [99] R. Wang et al., *Appl. Phys. Lett.* **86**, 052901 (2005).
- [100] X. Jiang et al., *Phys. Rev. Lett.* **94**, 056601 (2005).
- [101] S. Yuasa, T. Nagahama, A. Fukushima, Y. Suzuki, and K. Ando, *Nature Materials* **3**, 868 (2004).
- [102] S. S. P. Parkin et al., *Nature Materials* **3**, 862 (2004).
- [103] J. S. Parker, S. M. Watts, P. G. Ivanov, and P. Xiong, *Phys. Rev. Lett.* **88**, 196601 (2002).

- [104] D. Wang, C. Nordman, J. M. Daughton, Z. Qian, and J. Fink, *IEEE Trans. Magn.* **40**, 2269 (2004).
- [105] V. V. Rossin, P. C. M. Christianen, and V. V. Travnikov, *Semicond. Sci. Technol.* **9**, 716 (1994).
- [106] H. Sanada et al., *Appl. Phys. Lett.* **81**, 2788 (2002).
- [107] E. A. Barry, A. A. Kiselev, and K. W. Kim, *Appl. Phys. Lett.* **82**, 3686 (2003).
- [108] M. I. D'yakonov and V. Y. Kachorovskii, *Sov. Phys. Semi.-USSR* **20**, 110 (1986).
- [109] A. F. Panchula, *Magnetotransport in Magnetic Nanostructures*, PhD thesis, Stanford University, Stanford, CA, 2003.
- [110] G. Salis et al., *Appl. Phys. Lett.* **87**, 262503 (2005).
- [111] S. F. Alvarado and P. Renaud, *Physical Review Letters* **68**, 1387 (1992).
- [112] L. E. Golub, N. S. Averkiev, and M. Willander, *Nanotechnology* **11**, 215 (2000).
- [113] A. Ndirango, Personal correspondence with Dr. Anthony Dhirango, PhD, Department of Physics, University of California, Berkeley, CA, 2006 .
- [114] C. M. Wolfe, G. E. Stillman, and W. T. Lindley, *J. Appl. Phys.* **41**, 3088 (1970).
- [115] W. H. Lau, J. T. Olesberg, and M. E. Flatté, *Phys. Rev. B* **64**, 161301(R) (2001).
- [116] X. Jiang, *Spin Transport and Spin Injection in Tunnel Based Spintronic Devices*, PhD thesis, Stanford University, Stanford, CA, 2004.
- [117] F. G. Pikus and G. E. Pikus, *Phys. Rev. B* **51**, 16928 (1995).

- [118] M. Gurioli et al., Phys. Rev. B **44**, 3115 (1991).
- [119] J. Tignon et al., Phys. Rev. B **58**, 7076 (1998).
- [120] O. M. J. van 't Erve et al., Appl. Phys. Lett. **84**, 4334 (2004).
- [121] M. I. D'yakonov and V. I. Perel', Sov. Phys.-JETP **38**, 177 (1974).
- [122] N. S. Averkiev and L. E. Golub, Phys. Rev. B **60**, 15582 (1999).